JOURNAL OF GEOPHYSICAL RESEARCH, VOL. 105, NO. B4, PAGES 8205–8226, APRIL 10, 2000

Crustal thickness and structure along three contrasting spreading segments of the Mid-Atlantic Ridge, 33.5°-35°N

E. E. E. Hooft,[1,2] R. S. Detrick,[3] D. R. Toomey,[4] J. A. Collins,[3] and J. Lin[3]

Abstract. The crustal thickness and crustal and upper mantle structure along the rift valleys of three segments of the northern Mid-Atlantic Ridge with contrasting morphologies and gravity signatures are determined from a seismic refraction study. These segments lie between the Oceanographer and Hayes transforms and from north to south have progressively deeper axial valleys with less along-axis relief and smaller mantle Bouguer gravity lows. Major variations in seismic crustal thickness and crustal velocity and density structure are observed along these segments. The thickest crust is found near the segment centers, with maximum crustal thicknesses of 8.1, 6.9, and 6.6 ±0.5 km, decreasing from north to south. However, the mean crustal thickness is similar for each segment (5.6±0.4, 5.7±0.4 and 5.1±0.3 km). Near the segment ends, crustal thickness is 2.5 to 5 ±0.5 km with no systematic variation from north to south. At segment ends, both crustal velocities and vertical velocity gradients are anomalous and may indicate fracturing and alteration of thin igneous crust and underlying mantle. Away from segment ends, the thickness of the upper crust is relatively uniform along axis (~3 km), although its internal structure is laterally heterogeneous (velocity anomalies of ±0.6 km s^{-1} over distances of 5 km), possibly related to the presence of discrete volcanic centers. The along-axis crustal thickness variations are primarily accommodated in the lower crust. The center of the northern segment (OH-1) has an unusually thick crustal root (excess thickness of 2-4 km and along-axis extent of 12 km). Our results are consistent with an enhanced supply of melt from the mantle to the segment centers and redistribution of magma along axis at shallow crustal levels by lateral dike injection. Along this portion of the Mid-Atlantic Ridge, our results suggest that differences in axial morphology, seismic crustal thickness, and gravity anomalies are correlated and the result of variations in melt flux from the mantle. A surprising result is that the melt flux per segment length is similar for all three segments despite their different morphologies and gravity signatures. This argues against excess melting of the mantle beneath segment OH-1. Instead, we suggest that the thickened crust at the segment center is a result of focusing of melt, possibly due to the influence of the thermal structure of the Oceanographer fracture zone on melt migration in the mantle.

1. Introduction

Crustal formation at slow spreading ridges, like the Mid-Atlantic Ridge (MAR), is viewed as a three-dimensional, temporally variable process primarily governed by the nature of mantle flow and melt migration beneath the ridge axis and the variable thermal and mechanical properties of the lithosphere forming along a segment. This model is based on the integration of results from detailed geophysical mapping of off-axis magnetics [*Schouten and White*, 1980], bathymetry and gravity over portions of the MAR [*Crane*, 1985; *Lin et al.*, 1990; *Detrick et al.*, 1995], the distribution of lower crustal and upper mantle rocks recovered from the MAR rift valley and adjacent fracture zones [*Fox et al.*, 1976; *Dick et al.*, 1992; *Mutter and Karson*, 1992; *Cannat*, 1993], seismic refraction and microseismicity studies at the MAR ridge [*Toomey et al.*, 1985, 1988; *Purdy and Detrick*, 1986; *Kong et al.*, 1992; *Tolstoy et al.*, 1993; *Wolfe et al.*, 1995], and numerical, geochemical, and laboratory modeling of mantle flow and melt migration processes at ridge crests [*Whitehead et al.*, 1984; *Sempéré et al.*, 1990; *Sparks and Parmentier*, 1994; *Kelemen et al.*, 1995; *Kincaid et al.*, 1996; *Magde and Sparks*, 1997; *Reynolds and Langmuir*, 1997]. The supply of melt to the crust is predicted to be greater near segment centers, either due to plume-like, buoyantly-driven mantle upwelling [*Whitehead et al.*, 1984; *Lin and Phipps Morgan*, 1992] or three-dimensional melt migration in a more passive, plate-driven mantle flow [*Sparks and Parmentier*, 1993; *Sparks et al.*, 1993; *Magde and Sparks*, 1997; *Reynolds and Langmuir*, 1997]. This results in the formation of thick crust near segment centers and thinner crust near segment ends. Large, segment-scale variations in crustal thickness and axial thermal structure are also predicted to strongly affect both rift valley morphology and tectonics [*Chen and Morgan*, 1990; *Shaw*, 1992; *Neumann and Forsyth*, 1993; *Shaw and Lin*, 1996]. At the middle of a segment, thicker crust and thus thinner, warm lithosphere lead to a narrow, shallower rift valley and small-offset, closely spaced faulting. Thin crust

[1]Department of Terrestrial Magnetism, Carnegie Institution of Washington, Washington, D.C.
[2]Also at Department of Geological Sciences, University of Oregon, Eugene.
[3]Department of Marine Geology and Geophysics, Woods Hole Oceanographic Institution, Woods Hole, Massachusetts.
[4]Department of Geological Sciences, University of Oregon, Eugene.

Paper number 1999JB900442.
0148-0227/00/1999JB900442$09.00

and thick, cold axial lithosphere at segment ends allow a deep and wide rift valley and large, widely spaced faults to develop. Near segment ends, there is also evidence for low-angle detachment faulting in the cold, brittle lithosphere [*Mutter and Karson*, 1992; *Tucholke and Lin*, 1994; *Escartín and Lin*, 1995].

The discovery in the late 1980s of circular mantle Bouguer anomaly (MBA) gravity lows or "bull's-eyes" centered on spreading segments at the MAR and the inference from these anomalies of large, along-axis variations in crustal thickness [*Schouten et al.*, 1985; *Kuo and Forsyth*, 1988; *Lin et al.*, 1990; *Blackman and Forsyth*, 1991; *Morris and Detrick*, 1991; *Detrick et al.*, 1995] were key observational constraints in the development of this view of crustal accretion processes at the MAR. The MBA lows typically have wavelengths of 20-75 km, amplitudes of up to 50 mGal, and dimensions that are proportional to segment length [*Lin and Phipps Morgan*, 1992]. Although MBAs may arise from variations in crustal and upper mantle density, as well as variations in crustal thickness, these anomalies are typically interpreted as reflecting variations in crustal thickness. Segment-scale differences in crustal thickness of 2 to 3 km are predicted along the MAR [*Detrick et al.*, 1995]. However, the absolute crustal thickness and detailed pattern of distribution cannot be determined from gravity data. To date the only seismic refraction experiment to examine directly the relationship between MBA and crustal thickness variations is from the southern MAR near 33°S and 34°S [*Tolstoy et al.*, 1993]. The magnitude of crustal thickness variations along this portion of the MAR (3.5-8 km) was sufficient to explain the gravity bull's-eyes in this area, although it was found that the MBA underpredicted the amount of crustal thinning near segment ends because crustal thinning is accomplished primarily by variations in the thickness of the more dense seismic layer 3.

In this paper we present results from a seismic refraction experiment that determined seismic crustal structure and thickness variations, and upper mantle structure, at three contrasting segments along the northern MAR between 33° and 35°N. This experiment had three main goals: (1) to constrain the magnitude of crustal thickness variations along segments with very different MBA signatures, (2) to determine the relationship between crustal thickness variations and along-axis changes in axial morphology, and (3) to examine the relative contributions of crustal and upper mantle sources to the MBA observed at the MAR. We show that there are substantial along-axis variations in crustal thickness (3-6 km) within and between the three segments which can be directly correlated with the observed differences in axial depth and morphology. Along axis redistribution of melt at shallow crustal depths generates an upper crust with relatively uniform thickness. The MBA lows are consistent with the observed along-axis variations in crustal thickness and density. A surprising new result is that the mean crustal thickness is relatively uniform for all three segments. However, segment OH-1 has unusually thick crust at its center, pointing to an enhanced melt flux at the segment center relative to its ends, possibly due to the influence of the Oceanographer fracture zone on the migration of melt up sloping mantle isotherms.

2. Mid-Atlantic Ridge Between the Oceanographer and Hayes Fracture Zones

The Mid-Atlantic Ridge between the Hayes and Oceanographer fracture zones is segmented into three major spreading centers (OH-1, OH-2, and OH-3) with distinctly different axial morphologies (Figure 1) and gravity signatures (Figure 2) [*Detrick et al.*, 1995]. The half-spreading rate is 10-11 mm yr^{-1} [*LeDouaran et al.*, 1982; *DeMets et al.*, 1990]. The northernmost ridge segment (OH-1) is ~90 km in length and is bounded on the north by the Oceanographer fracture zone. Segments OH-1, OH-2, and OH-3 are separated by small (~35 km offset) nontransform discontinuities (NTO1 at 34°30'N and NTO2 at 34°00'N, respectively). Segment OH-1 has an hourglass-shaped rift valley. Near the center of the segment the inner valley floor is shallow (2200 m) and narrow (<4 km), and the rift valley relief is low (400 m). To the north and south the rift valley deepens (~4000 m at the northern end and ~3000 m at southern end) and widens (to 40 and 20 km). There is up to ~3 km relief at the ridge-transform inside corner. In contrast, segments OH-2 and OH-3 have more linear and deeper rift valleys that are ~60 km and ~45 km in length, respectively. The rift valley floor of segment OH-2 deepens from north to south (2900 to 3300 m), while segment OH-3 is generally deeper with a rift valley floor depth of 3000 m at the segment center and depths of 3600-3900 m at the segment ends. Segment OH-3 is bounded on the south by a small and recently developed nontransform offset (NTO3, offset ~15 km).

In terms of their gravity signature (Figure 2) the three spreading centers OH-1, OH-2, and OH-3 are also distinctly different [*Detrick et al.*, 1995]. Segment OH-1 has an unusually large negative mantle Bouguer gravity anomaly (MBA) (peak amplitude of about -60 mGal). The amplitude of the negative MBA at the segment center decreases from north to south (Figure 2b). After correcting for the thermal structure of the mantle due to three-dimensional passive, plate-driven flow [*Phipps Morgan and Forsyth*, 1988], the along-axis residual mantle Bouguer anomaly (RMBA) has an amplitude of -40, -25 and -20 mGal for segment OH-1, OH-2, and OH-3, respectively (Figure 2c). In terms of Moho topography [*Kuo and Forsyth*, 1988] these gravity anomalies predict along-axis crustal thickness variations of ~4, ~2.5, and ~2 km, respectively (Figure 2d).

This region of the MAR has been well studied with bathymetry and gravity mapping [*Needham et al.*, 1992; *Detrick et al.*, 1995; *Deplus et al.*, 1998], geochemical sampling [*Schilling*, 1986; *Shirey et al.*, 1987; *Schilling*, 1991; *Yu et al.*, 1997], submersible exploration [*Bideau et al.*, 1996; *Gràcia et al.*, 1997], and seismic studies [*Sinha and Louden*, 1983; *Barclay et al.*, 1998, also Microearthquake characteristics and crustal V_p/V_s structure at the Mid-Atlantic Ridge, 35°N, submitted to *Journal of Geophysical Research*, 1999, hereinafter referred to as Barclay et al., submitted manuscript, 1999; *Magde et al.*, 2000]. The French submersible *Nautile* observed evidence of recent volcanic activity near the center of the rift valleys of segments OH-1 and OH-3, while at the segment ends, evidence was found for tectonism and mantle exposures indicating thin crust [*Bideau et al.*, 1996; *Gràcia et al.*, 1997]. Geochemical studies suggest that segment OH-1 represents either a separate, weak plume (the Great Meteor) of Azores-type composition [*Schilling*, 1986; *Yu et al.*, 1997], melting of subcontinental lithosphere [*Shirey et al.*, 1987], or small-scale, spatial and temporal melting heterogeneities in the mantle [*Bideau et al.*, 1996]. Segment OH-1 is also characterized by a chain of large seamounts (up to 500 m in height above the surrounding seafloor) that intersects the ridge near the segment center [*Needham et al.*, 1992].

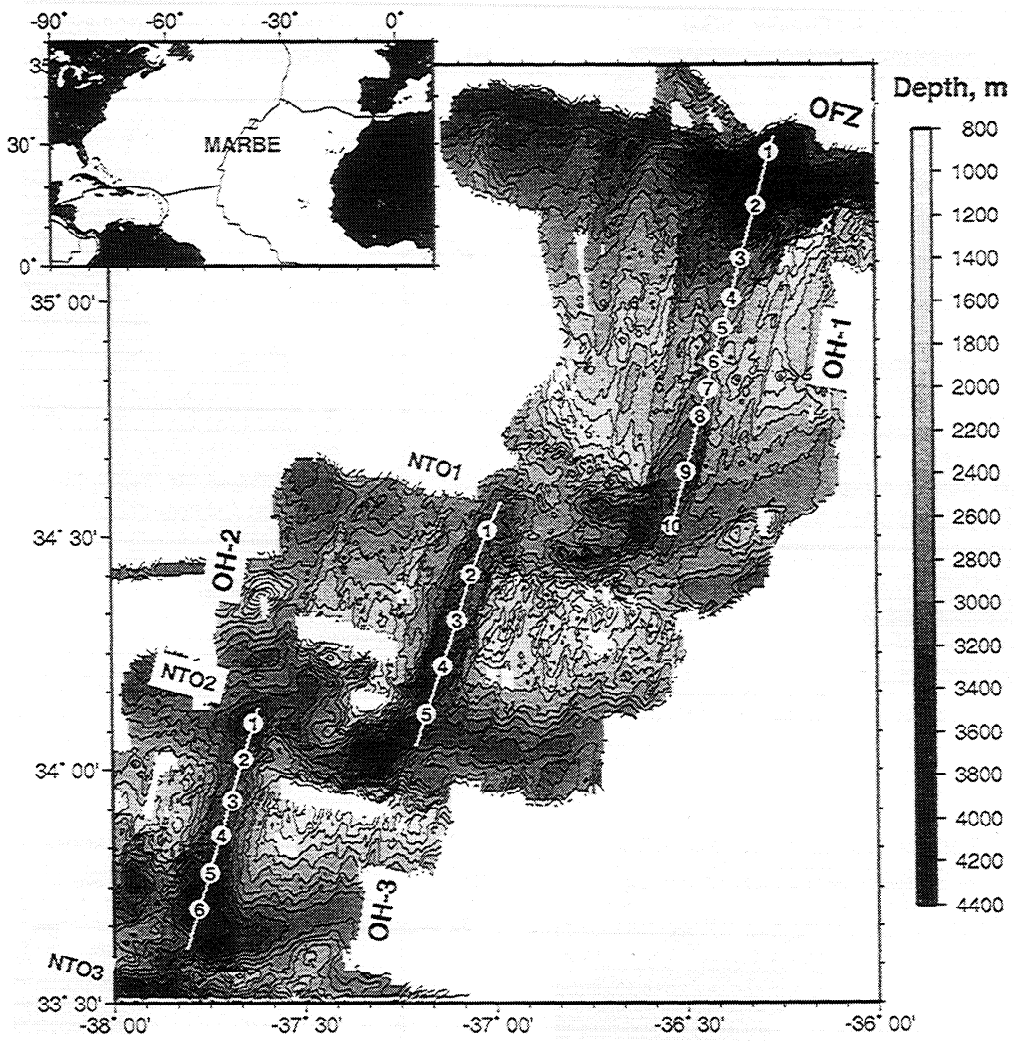

Figure 1. The bathymetric maps used in this paper integrate the multibeam bathymetry collected during this cruise with that of *Needham et al.* [1992]. Depth errors are ±10 m, and horizontal uncertainty is ±5 m. The location of the air gun shots for the three seismic refraction profiles are shown as lines along the rift valleys of the three spreading segments OH-1, OH-2, and OH-3. The ocean bottom hydrophones are shown as circles numbered according to the station location along each profile. The Oceanographer fracture zone (OFZ) and the three nontransform offsets (NTO1, NTO2, and NTO3) that delimit these segments are indicated.

3. Seismic Experiment and Data Processing

The Mid-Atlantic Ridge Bull's Eye Experiment (MARBE) was carried out in October/November 1996 on the MAR between the Oceanographer and Hayes fracture zones [*Detrick et al.*, 1997]. As part of this experiment, refraction profiles were shot along the rift valleys of segments OH-1, OH-2, and OH-3 (Figure 1). Two off-axis refraction profiles were shot; one located in the eastern rift mountains of segment OH-1 (A. Hosford et al., manuscript in preparation, 1999), and another in the western rift mountains of segment OH-1, crossing the non-transform offset NTO1, and following the eastern rift mountains of segment OH-2 [*Canales et al.*, 2000]. The data along segments OH-1, OH-2, and OH-3 were recorded during two deployments of 10 Woods Hole Oceanographic Institution (WHOI) ocean bottom hydrophones (OBHs) and one new Ocean Reftek in a Ball (ORB) hydrophone. The ORB is a new, small, and versatile seismic package which consists of a 24-bit Reftek 72A-07 data logger placed in a 17-inch (43-cm) glass ball which was deployed with a hydrophone attached to the hard-hat surrounding the glass ball. To minimize topographic effects in the rugged terrain at the Mid-Atlantic Ridge, the instruments and shots were located along the axial valleys of the three ridge segments. This geometry limited the experiment aperture to the segment length and thus constrained the maximum ray turning depth.

The 90-km-long refraction profile along the northern segment, OH-1, comprised 10 receivers spaced 7-15 km apart and 485 shots. Five stations spaced 12-15 km apart were located along OH-2 and recorded 301 shots, while there were six stations (five OBHs and one ORB) along OH-3, which also recorded 301 shots. The hydrophone sensors were floated 6 m above the seafloor; the sampling rate was 200 samples/s. The shots were from the R/V *Maurice Ewing* air gun array (8420 cubic inch or 138 L volume). The shot interval was 90 s which at a nominal ship speed of 4.2 knots gives a shot spacing of ~200 m. The guns were towed 10-12 m below the sea surface along OH-1 and 14-16 m below the sea surface along OH-2 and OH-3; the deeper values were due to strong tail currents. A linear clock drift correction was applied to the OBHs, and

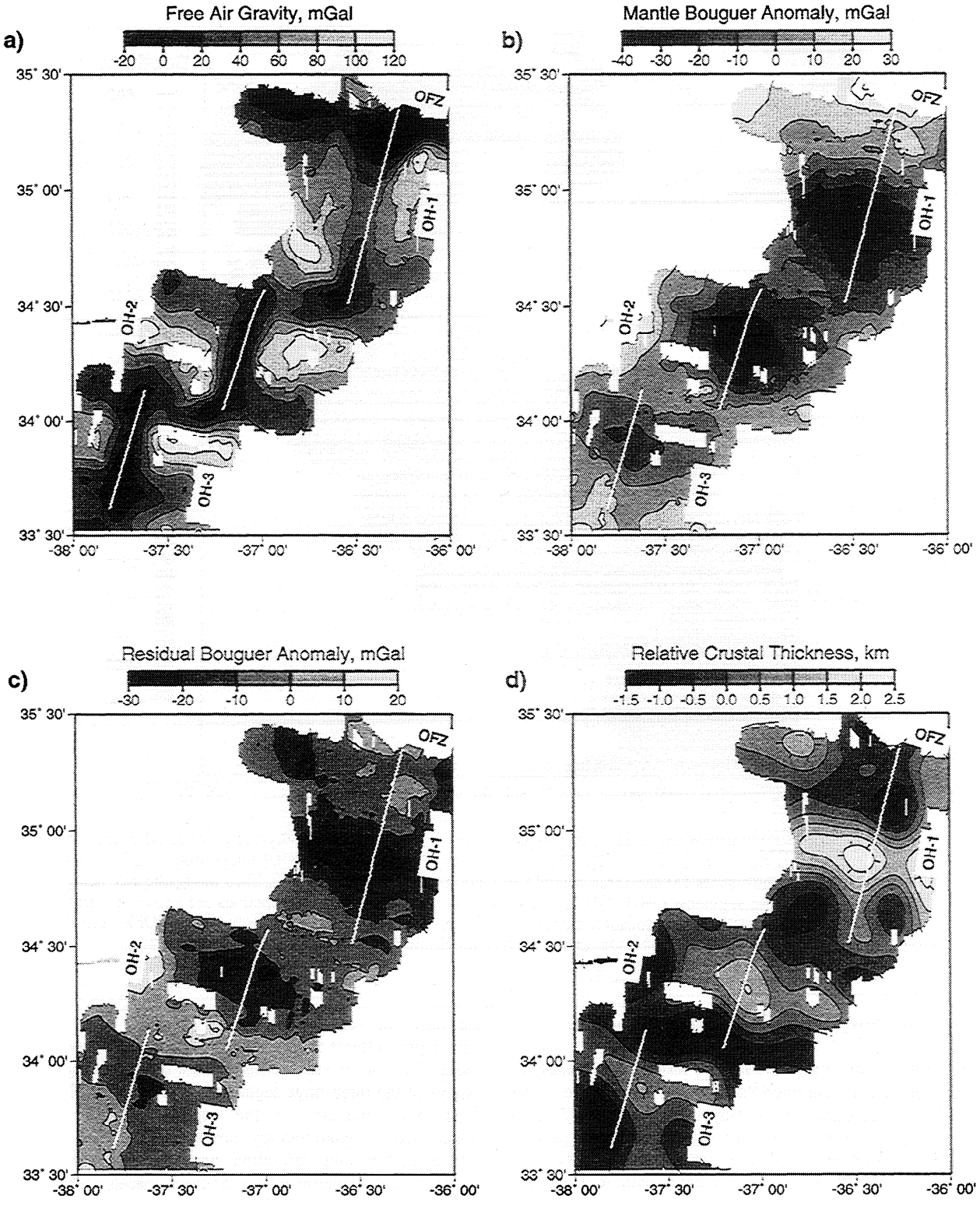

Figure 2. (a) The gravity anomaly and crustal thickness maps shown in this paper were constructed by integrating the free-air gravity data collected during the Mid-Atlantic Ridge Bull's Eye Experiment (MARBE) cruise with that of *Needham et al.* [1992]. (b) The mantle Bouguer anomaly and (c) the residual mantle Bouguer anomaly were constructed using the traditional approach [*Kuo and Forsyth*, 1988; *Phipps Morgan and Forsyth*, 1988; *Lin et al.*, 1990]. This removes the three-dimensional effect of the seafloor topography, an assumed crust-mantle boundary at 6 km below the seafloor, and the gravitational effect of mantle density changes due to the temperature field of a simple three-dimensional, plate-driven mantle flow model. The water, crustal, and mantle densities are assumed to be 1500, 2700, and 3300 kg m^{-3}, respectively, and the thermal expansion coefficient of the mantle is taken to be 3.4×10^{-5} $°C^{-1}$. (d) The crustal thickness is predicted from the residual mantle Bouguer anomaly by downward continuation to 7 km depth using the procedure of *Kuo and Forsyth* [1988]. The seismic refraction profiles along the rift valleys of segments OH-1, OH-2, and OH-3 are shown by lines.

instrument positions were determined from Global Positioning System (GPS) shot positions and water wave travel times using the method of *Creager and Dorman* [1982]. Instrument locations were better constrained along the north-south profiles (~5 m uncertainty) than in the cross-profile direction.

Data quality was generally very good (Figure 3). Refracted first arrivals (*Pg* and *Pn*) can be identified out to shot-receiver ranges of 40-50 km. Wide-angle reflections from the crust-mantle boundary (*PmP*) are frequently faint; these arrivals may be complicated due to topography on the crust-mantle interface, upper crustal heterogeneities, or a crust-mantle transition zone with a gradual velocity gradient. OBH25 along segment OH-1 shows the clearest *PmP* arrivals (Figure 3c). On the northernmost instrument of OH-1 (OBH23), a mantle refracted arrival (*Pn*) with an apparent velocity of ~8 km s^{-1} appears at small shot-receiver ranges, indicating thin crust just south of the Oceanographer fracture zone (Figure 3a).

To identify the first arrival travel times of crustal and mantle refracted waves (*Pg* and *Pn*), the seismic data were filtered from 5 to 40 Hz. The travel time picks were made manually, and the associated errors were estimated to be 5 to 70 ms with an average of ~23 ms. For identification of the lower frequency *PmP* phases, the data were filtered from 4 to 12 Hz, a spiking deconvolution was applied, and seafloor topography was removed using the water path travel times determined for the best fitting tomographic inversions. All errors in *PmP* picks were conservatively assigned to be 50 ms.

To determine the level to which a model should fit the data, we sum the estimated variances of all the uncertainties in a travel time observation. Sources of uncertainty, summarized in Table 1, include source and receiver positions, clock corrections, source time, identification of the arrival time, and bathymetry at the ray entry point. The final predicted uncertainty in first arrival times is 29 ms for segment OH-1 and ~25 ms for segments OH-2 and OH-3. The predicted uncertainty in *PmP* arrival times is 54 ms for OH-1 and 51 ms for OH-2 and OH-3. The largest source of uncertainty is the identification of the first arrival time and the location of the OBHs.

4. Methods and Results

4.1. Tomographic Inversions

The first arrival travel time data for the three rift valley seismic refraction lines were inverted to determine the two-dimensional crustal velocity structure using the tomographic technique of *Toomey et al.* [1994]. This tomographic method employs a shortest-path ray tracer [*Moser*, 1991] and an inversion that is stabilized by the addition of prior model covariance and smoothness constraints. The velocity model used for seismic ray tracing consists of finely spaced nodes (200 m in the vertical and horizontal directions) which are sheared vertically to conform to the bathymetry. The inversion solves for perturbations on a more coarsely sampled grid (1 km horizontally and 200 m vertically); between iterations the perturbational model is linearly interpolated and then added to the velocity model for ray tracing. The tomographic inversion weights individual travel times according to their estimated error. Further details are described by *Toomey et al.* [1994]. Table 2 summarizes the statistics of all the tomographic inversions.

The first arrival travel time data were initially inverted for the best fitting one-dimensional (depth-dependent) velocity model. Relative to the starting model, taken from *Purdy and Detrick* [1986] for the Mid-Atlantic Ridge at 23°N, these one-dimensional models reduce the root-mean-square (RMS) travel time misfit from 238 ms to 106 ms for OH-1, from 86 ms to 52 ms for OH-2, and from 147 ms to 72 ms for OH-3. These models have a χ^2 of 59.6, 9.4, and 10.3, respectively, where

$$\chi^2 = \frac{1}{N-1}\sum_{i=1}^{N}\left(\frac{t_{i,\mathrm{obs}} - t_{i,\mathrm{calc}}}{s_i}\right)^2 \quad (1)$$

and $t_{i,\mathrm{obs}}$, $t_{i,\mathrm{calc}}$, and s_i are the observed and calculated travel times and standard deviation for the ith of a total of N observations. The best fitting one-dimensional velocity model for each segment was then used as the starting model for two-dimensional velocity inversions. An intermediate solution was derived using a set of inversion parameters that yielded smooth, long-wavelength perturbations (~20 km). This model was then iteratively refined so that smaller-scale perturbations were imaged. The inversions were stopped when the RMS travel time residual was reduced to ~25 ms. This misfit approximately equals the total data uncertainty (Table 1). These models have χ^2 of 3.4, 4.1, and 1.1, for segments OH-1, OH-2, and OH-3, respectively.

The resolution of the velocity models may be approximated by the derivative weight sum (DWS), which is a weighted sum of the length of ray paths that influence a model parameter [*Toomey et al.*, 1990]. The velocity models were blanked out where the DWS was less than a predetermined cutoff value of 5. The DWS, however, does not accurately represent resolution as it does not take into account the angular distribution of ray paths. For example, at shallow depths where all rays were vertical and the vertical resolution is poor, the DWS is high. See the appendix for further discussion of model resolution.

4.2. Tomographic Results: Crustal Velocity Structure

The tomographically determined velocity and perturbational models are shown in Plates 1 and 2. Figure 4 compares velocity-depth structures averaged over along-axis distances of 10 km at the center and ends of the three segments. At the centers of the segments the velocity-depth profiles are typical of oceanic crust, though the velocities are generally higher than those obtained by *Purdy and Detrick* [1986] at 23°N on the MAR. Near the segment centers, seismic layer 2 is characterized by velocities increasing rapidly to ~5.5 km s^{-1} at 1.5 km depth below the seafloor and then more gradually to ~6.5 km s^{-1} at 3 km depth. Velocities (6.5-7.2 km s^{-1}) and gradual velocity gradients indicative of seismic layer 3 are present in the lower crust, except near the center of segment OH-1, where a velocity inversion of about -0.2 km s^{-1} is detected from 5 to 7 km depth. The presence of this velocity inversion is supported by a reduction in amplitude of the lower crustal refracted arrivals observed at coordinates 2-12 km on OBH25 (Figure 3c).

The velocity structure in the Oceanographer fracture zone is markedly different from that at the center of the segments (Figure 4a). The near-seafloor velocities are lower, and the velocity increases linearly with depth; a distinctive change in gradient associated with the seismic layer 2/3 boundary and the low-velocity gradients typical of layer 3 are not present (<1 km s^{-1} km^{-1} [*White et al.*, 1992]). The character of this velocity-depth profile is common at other large North Atlantic fracture zones [*White et al.*, 1984; *Detrick et al.*, 1993]. The velocity profiles from the nontransform offsets bounding

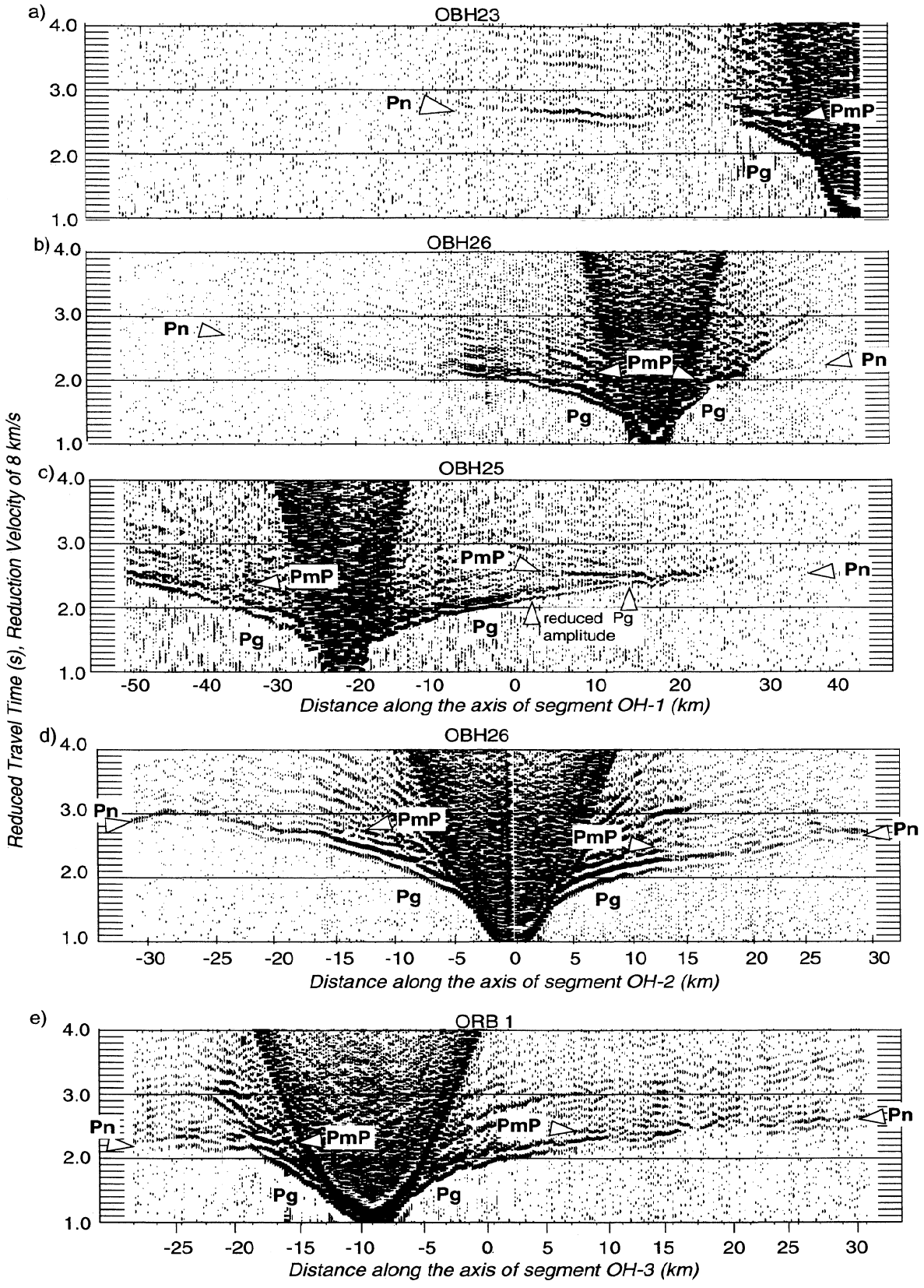

Figure 3. Five examples of ocean bottom hydrophone record sections from this experiment are shown. (a) to (c) Instruments OBH23, OBH26, and OBH25 are along segment OH-1 (stations 1, 3, and 8, respectively). (d) Instrument OBH26 is from segment OH-2 (station 3) and (e) instrument ORB1 is from segment OH-3 (station 5). The seismic data are filtered from 4 to 12 Hz, and a spiking deconvolution was applied. The record sections are reduced to 8.0 km s^{-1} and the effect of the seafloor topography has been removed (see text for explanation). *Pg*, *PmP*, and *Pn* arrivals are indicated. In Figure 3c, note the reduced amplitude of the lower crustal refracted arrivals on station OBH25, segment OH-1.

Table 1. Travel Time Uncertainty

Source of Error	Location Error, m	Timing Error, ms
Shot location	12	3
Shot depth	3	2
OBH location	65 (OH-1), 17 (OH-2 and OH-3)	19 (OH-1), 5 (OH-2 and OH-3)
OBH depth	15	4
Ray entry point bathymetry	10	3
Clock drift	--	<1
Picking of first arrivals	--	22 (OH-1), 23 (OH-2), 24 (OH-3)
Picking of *PmP* arrivals	--	50
Shot origin time	--	<1
Total, first arrivals		29 (OH-1), 24 (OH-2), 25 (OH-3)
Total, *PmP* arrivals		54 (OH-1), 51 (OH-2 and OH-3)

All uncertainties are one standard deviation. The OBH location uncertainty is the mean of the uncertainty ellipse of each individual OBH location.

segments OH-2 and OH-3 display a similar pattern of a linear velocity gradient with depth, anomalously low near-seafloor velocities, and thin crust (Figures 4b and 4c). At the southern end of segment OH-1, velocity gradients are not as linear, though velocities down to 5 km depth are clearly reduced relative to those at the segment center.

Away from the segment offsets, the thickness of the upper crust (velocities <6.5 km s^{-1}) is relatively uniform along the axis of the rift valley (Plates 1a, 2a, and 2c), however, the internal structure of the upper crust is heterogeneous. A plot of velocity perturbations relative to the average velocity-depth profile for each segment (Plates 1b, 2b, and 2d) reveals significant structural variability within the upper crust, especially along the rift valley of segment OH-1 where there are four to six high-velocity regions in the upper 3 km of the crust (+0.4 to +0.6 km s^{-1} over lateral distances of 5 km). These upper crustal velocity anomalies are well-resolved, and any velocity variations in the shallowest crust (from the seafloor to 500 m depth) do not generate artificial structure at depths >1 to 2 km (see the appendix for details). In contrast, only one such high-velocity zone is imaged along segments OH-2 and OH-3. Along segment OH-1, the high-velocity body at coordinate -8 km coincides with a velocity anomaly imaged in a detailed tomography study of the center of this segment [*Barclay et al.*, 1998]. Regions of anomalously low crustal velocity were detected away from the segment ends at OH-1 and OH-3 (-0.2 to -0.4 km s^{-1}, between 1 and 2 km depth and extending ~5 km along axis). At the center of segment OH-1, *Barclay et al.* [1998] imaged a low-velocity body of radius ~1 km between 1 and 2 km depth. This body was centered 4 km west of the seismic line shot in this study and therefore was not detected.

4.3. Modeling of *PmP* and *Pn* Arrivals

Crustal thickness along the axial valleys was determined using a two-dimensional ray-tracing technique [*Zelt and Smith*, 1992] to iteratively forward model wide-angle reflections from the crust-mantle boundary (*PmP* arrivals) and mantle turning rays (*Pn*). Velocity contours were extracted from the tomographically derived models at a contour interval of 0.2 km s^{-1} and 1-km horizontal spacing and used as interfaces for the crustal layers required by the method of *Zelt and Smith* [1992]. The seafloor interface was densely parametrized (200-m horizontal spacing). Initially, the Moho was assigned to the 7.2 km s^{-1} contour, and the mantle velocity was taken as 7.8 km s^{-1}. The shape of the Moho boundary and the mantle velocity were then iteratively modified to match the crustal arrivals and the mantle reflected and refracted arrivals.

For our forward ray trace modelling, the statistics of the different phases for each ridge segment are given in Table 3. The RMS travel time residual for all the phases was 45 to 47 ms with χ^2 values of 6.3, 3.8, and 3.7. Owing to the limitations of the ray shooting method, 10-20% fewer *Pg* and *Pn* phases were included in the forward modelling than in the tomographic inversions. The RMS travel time residual for the refracted phases is 44 to 46 ms, which is greater than the misfit for the tomography model (~25 ms). This difference is due to the more limited ability to represent structure, especially velocity inversions, in the forward ray shooting method than in the tomography method. We fit the *PmP* arrivals well with RMS travel time residuals of 39, 55, and 47 ms and χ^2 values of 0.6, 1.2, and 0.9 for segments OH-1, OH-2, and OH-3, respectively.

Table 2. Statistics for Tomographic Models

	Segment		
	OH-1	OH-2	OH-3
Number of travel time picks (*Pg* and *Pn*)	3208	1071	1285
RMS travel time misfit compared to PD, ms	238	86	147
Best 1-D Model			
RMS travel time residual, ms	106	52	72
χ^2	59.6	9.4	10.3
Best 2-D Model			
RMS travel time residual, ms	26	25	24
χ^2	3.4	4.1	1.1

PD is the velocity-depth structure determined by *Purdy and Detrick* [1986] for the Mid-Atlantic Ridge at 23°N.

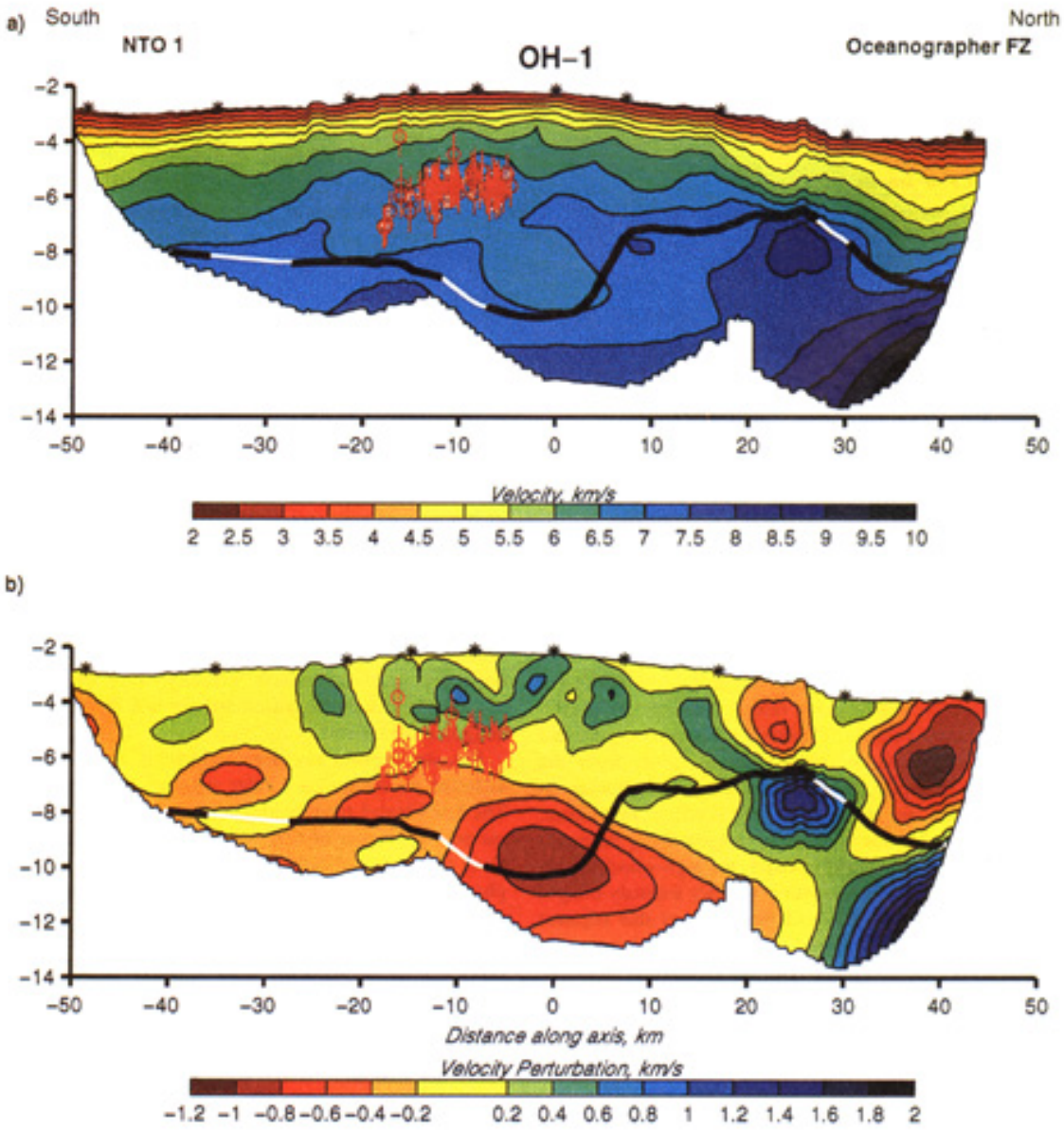

Plate 1. Two-dimensional velocity and perturbation models are determined for segment OH-1. (a) The velocity model is "hung" from the seafloor bathymetry along the axis of the rift valley and is masked where the DWS value is below 5. The locations of the ocean bottom hydrophones are shown by stars. (b) Perturbations of the velocity model relative to the depth-dependent average of this model are shown. Micro-earthquakes located by Barclay et al. (submitted manuscript, 1999) during a small, focused seismic experiment located between -18 and -2 km are shown as red circles with errors. The seismic Moho as determined from modelling of *PmP* reflections is shown as a black line; interpolated gaps are shown by white lines.

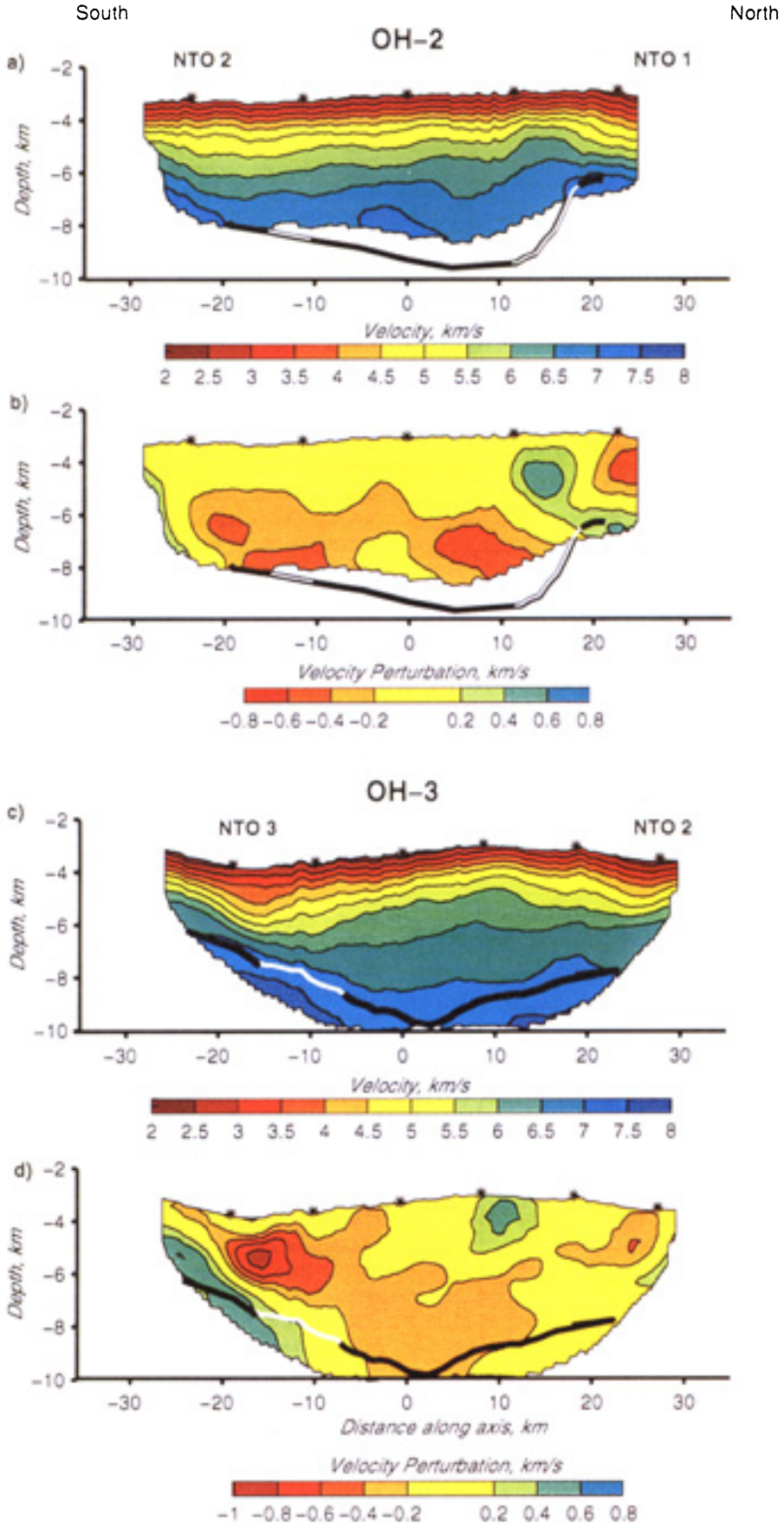

Plate 2. Two-dimensional velocity and perturbation models are determined for (a) and (b) segment OH-2; and (c) and (d) segment OH-3. See caption of Plate 1 for explanation.

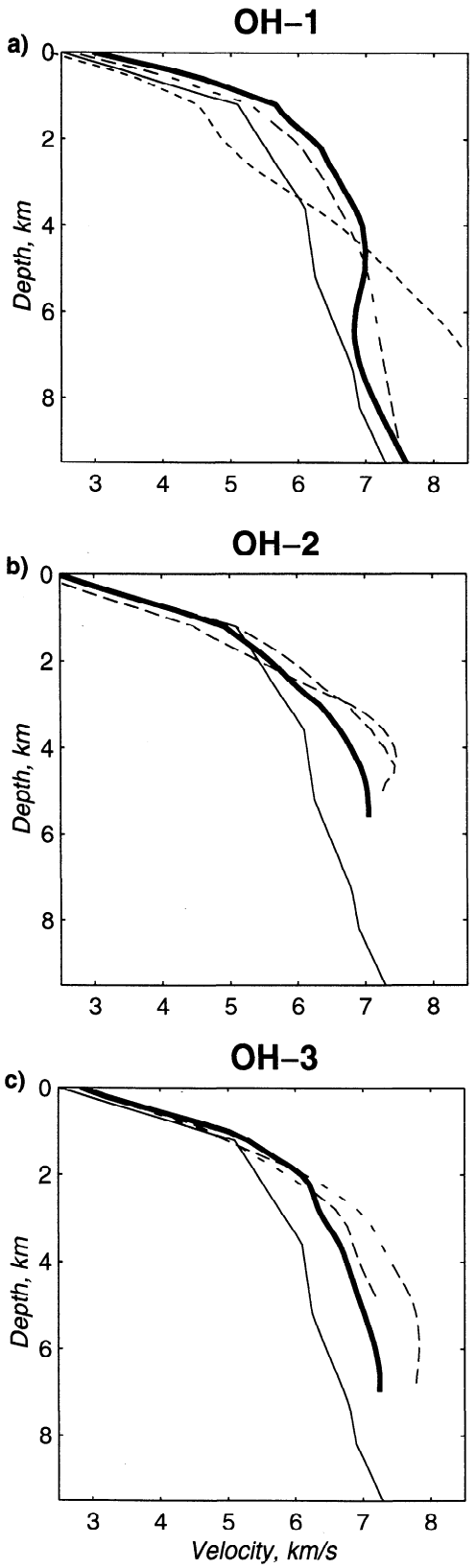

Figure 4. Velocity-depth profiles averaged laterally over 10 km through different geologic regions of the best fitting two-dimensional velocity models presented in Plates 1 and 2 are shown (the segment centers, heavy solid line; the nontransform offsets, long dashed line; and the Oceanographer fracture zone, short dashed line) for (a) OH-1, (b) OH-2, and (c) OH-3. The velocity structures are compared with the *Purdy and Detrick* [1986] velocity model from 23°N on the Mid-Atlantic Ridge (thin solid line).

4.4. Results From *PmP* and *Pn* Modeling: Crustal Thickness and Upper Mantle Velocities

Our final best fitting velocity models and the portions of the crust-mantle interface that are constrained by *PmP* reflections are shown in Plate 3. In contrast to the relatively uniform thickness of the upper crust, the lower crust (velocities > 6.5 km s^{-1}) accommodates most of the variation in crustal thickness along the axis of the three ridge segments (Plates 1a, 2a, and 2c). Crustal thickness at the center of the three segments decreases from north to south; it is 8.1, 6.9, and 6.6 ±0.5 km at the center of segments OH-1, OH-2, and OH-3, respectively (Table 4). Crustal thickness at the segment ends ranges from 2.5 to 5 ±0.5 km and does not vary systematically from north to south or with segment offset. In spite of the changes in crustal thickness at the segment centers the average crustal thickness per segment is relatively uniform at 5.6±0.4, 5.7±0.4, and 5.1±0.3 km for OH-1, OH-2, and OH-3, respectively. The mean crustal thickness was averaged from segment end to end along that part of the axis where the Moho was seismically constrained (see Table 4 for details and errors). This average ignores the possible effects of serpentinization at the segment ends on the volume of igneous material. In the extreme of no igneous crust at the segment ends, the mean crustal thickness would be reduced by ~1.6 km, but the intersegment variation in mean crustal thickness remains nearly the same.

The *PmP* modeling confirms that the crust thickens abruptly at the center of segment OH-1 to form a pronounced crustal root 8.1±0.5 km thick (an excess thickness of 2-4 km) between coordinates -10 and 2 km. Segment OH-1 differs from OH-2 and OH-3 because the crustal thickness at the segment center is greater (8.1 km versus 6.9 and 6.6 ±0.5 km) and because it has a more variable crustal thickness along the axis (standard deviation of the mean is 1.3 km versus 1.0 and 1.1 km for OH-2 and OH-3). These crustal thickness variations are consistent with morphologic and gravity indications that maximum crustal thickness decreases from north to south and that there are significant along-axis changes in crustal thickness within each individual segment [*Detrick et al.*, 1995].

The average subaxial mantle velocity along all three segments is 7.4 km s^{-1}, except for an increase to 7.8 km s^{-1} beneath the Oceanographer fracture zone. (Note that in this study the mantle turning rays only penetrate a few hundred meters beneath the Moho (Plate 3).) The 7.4 km s^{-1} mantle velocity is significantly lower than values measured off axis (7.8 km s^{-1}) [*Sinha and Louden*, 1983; *Canales et al.*, 2000] and comparable to that observed beneath the axis of the East Pacific Rise (7.3 km s^{-1}) [*Dunn and Toomey*, 1997]. This mantle velocity is also similar to the low mantle velocity (7.2-7.5 km s^{-1}) measured at the axis of the Mid-Atlantic Ridge in early seismic refraction studies [*Keen and Tramontini*, 1970; *Fowler*, 1976, 1978]. Increases in the velocity of the mantle as it moves off axis are expected due to cooling of the mantle. Similarly, higher mantle velocities south of the Oceanographer fracture zone (7.8 km s^{-1}) are probably due to cooling of the mantle against cold lithosphere across the fracture zone.

4.5. Gravity Anomalies

We used the seismic crustal structure to calculate the contribution of crustal density variations to the observed free-air gravity anomaly. Crustal seismic velocities were

Table 3. Statistics for Ray Trace Models

	Segment		
	OH-1	OH-2	OH-3
PmP Arrivals			
Number of travel time picks used	521	252	254
RMS travel time residual, ms	39	55	47
χ^2	0.6	1.2	0.9
Pg and Pn Arrivals			
Number of travel time picks used	2,790	920	978
RMS travel time residual, ms	46	45	44
χ^2	7.4	9.5	4.5
All Pg, Pn, and PmP Arrivals			
Number of travel time picks used	3311	1172	1232
RMS travel time residual, ms	45	47	45
χ^2	6.3	3.8	3.7

converted to density using the *Carlson and Raskin* [1984] velocity/density relation for oceanic rocks that takes into account the porosity of layer 2:

$$\rho\ (\text{Mg m}^{-3}) = (3.81 \pm 0.02) - (5.99 \pm 0.11) / V_p\ (\text{km s}^{-1}) \quad (2)$$

To approximate the gravitational effects of the axial valley topography, we extended the inferred densities 40 km perpendicular to the refraction profile, and 10 km to the north and south, and suspended this density model from the bathymetry following the method of *Canales et al.* [2000]. The positions of isodensity surfaces at 70 kg m^{-3} intervals within the crust were determined and assigned this density contrast. To avoid spatial aliasing, these density interfaces were mirrored on all sides. The gravitational effect of each of these surfaces was calculated using the spectral method of *Parker* [1972] and summed to give the gravitational contribution of the intracrustal density anomalies and the seafloor topography. This crustal gravity signature and the mantle density variations due to the thermal structure of three-dimensional, plate-driven mantle flow [*Phipps Morgan and Forsyth*, 1988] were subtracted from the observed free-air gravity anomaly to obtain the residual crustal Bouguer anomaly (RCBA). Variations in the RCBA may be attributed to topography on the crust-mantle interface and/or density variations in the mantle (other than due to the predicted mantle temperature based on a passive upwelling model) (Figure 5).

In order to assess the contribution of Moho topography to the RCBA, Figure 5 also shows the predicted gravitational effect of variations in crustal thickness. As in the RCBA calculation, the Moho topography determined from the ray trace forward modelling was extended perpendicular to the profile and suspended from the seafloor topography. The density anomaly across the Moho is from a lower crustal gabbro to a mantle density (2954 kg m^{-3} vs. 3300 kg m^{-3}, respectively). The gravitational effect of this surface is again calculated using the spectral method of *Parker* [1972].

4.6. Results From Gravity Anomalies: Crustal Thickness and Upper Mantle Structure

Along segment OH-1, an RCBA gradient of 35 mGal is consistent with significant Moho topography and/or low densities in the seismically defined mantle. In contrast, the RCBA gradients along segment OH-2 and OH-3 are less pronounced (15 mGal for both segments), consistent with lower relief on the Moho and/or more uniform mantle densities. Figure 5 shows that the gravitational effect of the seismic Moho does not fully account for the observed RCBA, with RMS misfits of 6.1, 5.1, and 2.8 mGal for segments OH-1, OH-2, and OH-3, respectively (Table 5). For example, at segment OH-1 the seismically determined crust does not produce a sufficient gravity gradient from the segment center to ends.

There are three possible explanations for the discrepancies between the observed RCBA and the predicted gravitational effect of the seismic Moho: (1) the segment ends are serpentinized and this is not taken into account in the velocity to density conversion, (2) there are low mantle densities beneath the center of the segments, and (3) the crustal thickness at the ends of the segments is poorly constrained. A velocity/density relation appropriate for partial serpentinization of peridotites [see *Canales et al.*, 2000] gives higher densities for velocities >6.5 km s^{-1}. However, this can only account for 3-5 mGal of the observed gravity difference at the segment ends (~15 mGal at segment OH-1). The second possibility is to reduce the gravity at the center of segment OH-1 by lowering the mantle density with higher temperatures and/or melt. However, the magnitude of the observed gravity low requires an unreasonably large volume of melt (200-300 km^3) to be present at shallow depths in the mantle (15-30 km). The last alternative is to modify the crustal thickness at the ends of the segments where the seismic Moho is poorly constrained. These changes to the boundary conditions of the gravity model reduce the RMS gravity misfit to 1.5-2.4 mGal for the three segments (Table 5 and Figure 5).

At segment OH-1, modification of the Moho topography at the ends of the segments to better match the RCBA leads to discrepancies with the seismically observed Moho (Plate 3). In particular, at the Oceanographer fracture zone the seismic Moho is up to 3 km thicker than that which fits the gravity data. This difference could be due to (1) poor *PmP* picks on the two northernmost stations of this refraction profile; (2) artificially thick crust due to incorrectly low crustal velocities within the fracture zone nodal basin; (3) some melt present in the mantle beneath the center of this segment may explain the large along-axis gradient in RCBA; (4) incorrect treatment of the seafloor or Moho topography or crustal density structure beyond the ends of this complicated ridge-transform intersection. Options 1, 2, and 3 are unlikely as the *PmP* picks appear to be good; the reduction in upper crustal velocities at the fracture zone is not large enough for the required amount of crustal thickness difference, and, as stated above, an unreasonably large amount of melt would be required for option 3. In the RCBA calculation, care was taken to include topography to 40 km off axis and 10 km to the north

Table 4. Crustal Thickness, Gravity, and Segment Geometry

Segment	Maximum Crustal Thickness, km	Mean Crustal Thickness, km	Standard Deviation of Mean, km	Axial Variation in RCBA, mGal	Segment Length, km	Maximum Offset Length, km
OH-1	8.1 ±0.5	5.6±0.4	1.3	35	90	120
OH-2	6.9 ±0.5	5.7±0.4	1.0	15	60	45
OH-3	6.6 ±0.5	5.1±0.3	1.1	15	45	30

For the maximum crustal thickness the error is the estimated uncertainty in the measurement. The mean crustal thickness is averaged from segment end to end along the axis where the Moho was seismically constrained, that is, from coordinates -40 to 35 km, -22 to 22 km, and -18 to 25 km, for segments OH-1, OH-2, and OH-3, respectively. The quoted errors are those due to the combined effect of the lack of *PmP* reflections at the segment ends (at segment OH-2), uncertainties in the definition of the segment end locations (±5 km), and inconsistencies between the seismic Moho and the Moho adjusted to satisfy the gravity data (at segment OH-1). The formal error of the mean is much smaller than these other sources of error. RCBA, residual crustal Bouguer anomaly.

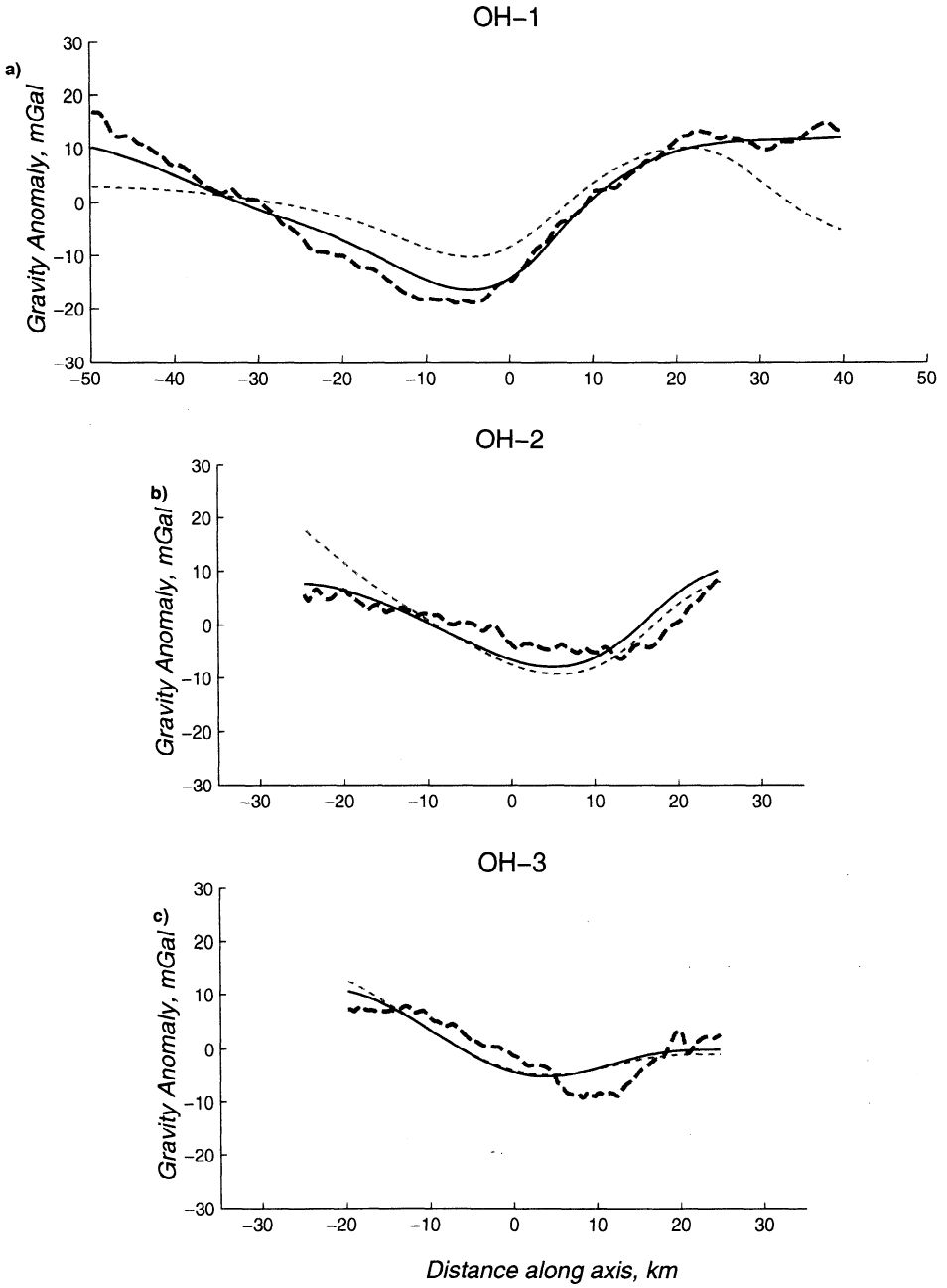

Figure 5. Along-axis plots are shown for the three segments (a) OH-1, (b) OH-2, and (c) OH-3 of the residual crustal Bouguer anomaly (RCBA; heavy dashed line) and the predicted gravitational effect of Moho topography. The light dashed lines show the predicted gravity for a Moho constrained by the seismic analysis (see Plate 3). The light solid lines show the predicted gravity after making adjustments to the Moho topography near the ends of the segments. See text for details.

of the profile. However, there remain uncertainties in the Moho topography and crustal density structure beyond the ends of the density model. This is the most likely source of the differences between the seismic Moho and that adjusted at the segment ends to fit the gravity data. The effect of this discrepancy has been incorporated in the error determinations for the average crustal thickness (Table 4).

Table 5. Misfit of Gravity Predicted from Moho Topography Compared to Residual Crustal Bouguer Anomaly

Segment	Seismic Moho, mGal	Adjusted Moho, mGal
OH-1	6.1	1.5
OH-2	5.1	2.3
OH-3	2.8	2.4

RMS misfit is calculated for the difference between the gravity predicted from Moho topography and the residual crustal Bouguer anomaly calculated from the free-air gravity data.

5. Interpretation

5.1. Upper Crustal Velocity Variations: Evidence for Shallow Intrusive Bodies

Away from the ends of segments, anomalously low velocities in the upper 1.5 km of the crust are most evident along segment OH-3 (coordinate -1 to -5 km). Anomalous *P* wave velocities in the upper crust cannot be interpreted uniquely since many effects come into play, including bulk porosity, grade of alteration, thermal structure, and lithology. However, other geological and geophysical observations provide additional constraints. Since the low-velocity feature at segment OH-3 coincides with the location of recently erupted lavas (33°49-52') [*Gràcia et al.*, 1997], we suggest that the anomalously low velocities are the result of elevated temperatures due to recent emplacement of a magma body. This postulated intrusive body is similar in size and depth to a low-velocity feature imaged beneath an axial seamount at the center of segment OH-1, which was interpreted to be a magma body with elevated temperatures and a few percent partial melt [*Barclay et al.*, 1998].

At depths <3 km, regions of anomalously high velocity (0.2-0.6 km s^{-1} and ~5 km horizontally) may represent cooled and relatively intact intrusions and thus yield an estimate of the size of magmatic bodies within the axial valley. Similar features have been observed in other geologic settings. For example, beneath the Hengill volcanic system in Iceland, high-velocity regions of ~1 km dimension are imaged shallower than 5 km and are associated with frozen and unfractured intrusions [*Toomey and Foulger*, 1989]. On a larger scale (~20 km), high-velocity structures have been imaged beneath volcanic centers in Iceland (at depths of 4-8 km) [*Brandsdóttir et al.*, 1997] and beneath Kilauea in Hawaii (to depths of 5-7 km and ~10 km wide) [*Okubo et al.*, 1997] and are interpreted as intrusives located in the rooting zones of volcanic systems. Within our study area, anomalously high-velocity, shallow crustal anomalies are particularly evident within segment OH-1. In view of the distinct volcanic features observed within the inner valley floor, these lateral velocity anomalies support temporally and spatially discrete magmatic bodies.

5.2. Segment Ends: Cracking, Alteration, and Tectonic Thinning

The low seafloor velocities and linear increase of velocity with depth observed in the Oceanographer fracture zone are probably the result of fracturing and alteration of a basaltic carapace overlying serpentinized peridotites. The velocity characteristics observed at the Oceanographer fracture zone intersection are commonly attributed to a dominant role of alteration and cracking rather than lithology and are typical of fracture zones (see *Detrick et al.* [1993] for a review). Serpentinization and fracturing of mantle material lying at shallow depths in the fracture zone nodal basin may reduce the velocities in the mantle to crustal values.

Near the nontransform offsets, the velocity-depth functions show similar characteristics, except that the depth extent of the linear velocity gradient is less than for the Oceanographer fracture zone (3 km versus 5 km, respectively). The nontransform velocity structures do not vary with offset size or from north to south. This suggests that the velocity-depth relation at segment ends constrains a common depth of fracturing and alteration rather than the thickness of the igneous section. In support of our interpretation, geological observations on segment OH-3 revealed broad, dome-like, serpentine and dolerite massifs at the nontransform intersections [*Gràcia et al.*, 1997] consistent with fracturing, alteration, and low-angle detachment faulting.

Thinning of the crust at segment ends is often attributed to reduced magmatic flux and tectonic extension. The diminished magma supply results in a colder thermal structure and allows the development of larger faults [*Shaw and Lin*, 1993]. We suggest that the shallow mantle (3 km depth) observed at the northern end of segment OH-1 (Plate 3) may be due to both a reduced magma supply and to tectonic unroofing on a large detachment fault at the Oceanographer eastern inside corner. Slip along a low-angle detachment would bring mantle up to shallow depths beneath the rift valley [e.g., *Mutter and Karson*, 1992; *Tucholke and Lin*, 1994].

5.3. Lower Crustal Velocities: Evidence for Partial Melt

Lower crustal velocities are generally more uniform than in the upper crust except in the crustal root at the center of segment OH-1, where a velocity inversion suggests the presence of partial melt. A comparison of on- and off-axis lower crustal root velocities (7-7.2 versus 7.4-7.6 km s^{-1} from 5-8 km depth) shows an average contrast of 0.4-0.5 km s^{-1}. If we assume that cooling of the crustal root with age is the cause of the average velocity contrast, this suggests that the on-axis lower crust is 700-900°C hotter (for $1/V_0 \cdot \delta V_p/\delta T = -8.1 \times 10^{-5}$ K^{-1} [*Christensen*, 1979] for V_O=7.0 km s^{-1}). Given that the off-axis lower crustal temperature is likely to be at several hundred degrees Celsius, it is probable that the root on axis is partially molten. In concert with this inference, our tomographic results indicate that a velocity inversion with depth is consistent with the data. Although this feature is not robustly resolved by axis-parallel data, it is substantiated by a shadow zone for rays passing through the crustal root (Figure 3c).

6. Discussion

6.1. Average Crustal Thickness: Implications for Mantle Melt Production

Seismic measurements of crustal thickness constrain the flux of melt from the mantle to the crust. A surprising result from this study is that our measurements of average crustal

thickness show that the melt flux (volume of melt per unit time) per segment length is effectively uniform, particularly if a long-wavelength regional trend is taken into consideration (Table 4). A regional trend in crustal thickness (a decrease of 0.5 km deg^{-1} of latitude from north to south) is expected due to the waning influence of the Azores hotspot on melting beneath the MAR [*Detrick et al.*, 1995]. This trend is consistent with the measured north-south decrease in mean crustal thickness (5.6±0.4 to 5.7±0.4 to 5.1±0.3 km over 1° of latitude).

The production of a similar melt flux per segment length has specific implications for models of mantle upwelling and melting. In the context of an actively upwelling mantle [*Whitehead et al.*, 1984; *Lin and Phipps Morgan*, 1992] the observed invariance in average crustal thickness requires a direct relationship between segment length and the amount of melt delivered by a mantle diapir. This is in agreement with earlier studies along the MAR which interpreted the correlation between MBA amplitude, segment length, and offset length [*Lin et al.*, 1990; *Detrick et al.*, 1995] to indicate a relationship between segment size and mantle diapir size [*Lin et al.*, 1990]. In this case, centrally thickened crust is generated by vertical ascent of melt from a mantle diapir.

Alternatively, the observed uniform average crustal thickness may indicate that segment length and offset do not affect the volume of melt produced per segment length. This may be expected since the penetration depth of the conductive boundary layer affects only the upper part of the melting column, which because of its geometrical shape is volumetrically small. Geochemical and petrologic studies and mantle flow models at the Mid-Atlantic Ridge support the idea that only the thermal perturbation of large transform offsets significantly truncates the melting column, while nontransform offsets overlie a continuous melting regime [*Magde and Sparks*, 1997; *Reynolds and Langmuir*, 1997]. In this scenario, migration of melt toward the segment center is required to generate the observed intrasegment variation in crustal thickness from a relatively continuous mantle melting regime [*Sparks and Parmentier*, 1994; *Magde et al.*, 1997; *Reynolds and Langmuir*, 1997]. Without new seismic information on the structure of the mantle beneath slow spreading ridge segments we cannot assess the relative importance of dynamic and passive forces in mantle upwelling.

6.2. Intrasegment Crustal Thickness Variations: Implications for Crustal Melt Transport

Our results confirm that along slow spreading ridges the magma flux from the mantle to the crust is greatest toward the center of a segment [e.g., *Schouten et al.*, 1985; *Kuo and Forsyth*, 1988; *Lin et al.*, 1990; *Tolstoy et al.*, 1993]. Although we cannot constrain the cause of the enhanced melt flux at the segment centers, we can address the fate of a variable melt supply as it enters the crust. There are two possibilities for how melt is transported within the crust: (1) melt moves vertically, or (2) melt is laterally redistributed.

Our results from segment OH-1 indicate that melt is redistributed or defocused at midcrustal depths. Thicker crust clearly indicates that the greatest volume of melt enters the crust at the segment center. With respect to crustal architecture this results in a lower crust which is thickest at the segment centers. Evidence for a velocity inversion in the crustal root at segment OH-1 suggests that the root on axis is partially molten. Overlying the crustal root a vertical zone of anomalously low velocities is recovered at depths of 3 to 5 km in three-dimensional tomographic images (~0.4 km s^{-1}, <15 km diameter) [*Magde et al.*, 2000]. These observations indicate that in the lower crust melt remains concentrated at the segment center and migration is primarily vertical.

While melt is concentrated at the segment center in the lower crust, at shallow crustal levels it is redistributed toward the segment ends. This generates the observed uniform thickness upper crust (velocities <6.5 km s^{-1}). Shallower than ~3 km, the low velocity anomaly imaged by *Magde et al.* [2000] becomes axis parallel (~44 km long) and above 2.5 km discrete low-velocity regions are imaged. These shallow features are associated with individual accretionary units on the rift valley floor, and *Magde et al.* [2000] interpret these low velocities as the magma plumbing system. The depth at which the magma plumbing system begins to spread out along axis appears to correspond to the maximum depth of microearthquakes (the brittle-ductile transition, ~3.5 km) (Barclay et al., submitted manuscript, 1999). These earthquakes lie at the top of the lower crust (velocities 6.6 to 6.8 km s^{-1}) and their depth corresponds to the transition in our images from shallow lateral velocity perturbations, to deeper more uniform velocities (Plate 1). This suggests that there may be a rheological boundary that controls the change in crustal melt transport from dominantly vertical to more horizontal. Shallow level redistribution of melt may be occurring through extensive lateral dike propagation (tens of kilometers) as has been observed along the CoAxial segment of the Juan de Fuca Ridge [*Dziak et al.*, 1995], the Kilauea rift zone [*Koyanagi et al.*, 1988; *Rubin et al.*, 1998], and along Icelandic fissure swarms [*Einarsson and Brandsdóttir*, 1980].

6.3. Ridge Morphology and Crustal Thickness

Our results indicate that along-axis variations in crustal thickness influence axial depth and the characteristic morphology of the rift valley [*Neumann and Forsyth*, 1993]. However, the extent of such influence is variable, suggesting that factors beyond crustal thickness are also important. Since seismic crustal thickness measurements average laterally over ±2 km at Moho depths they represent the average magma flux over intervals of 10^5 years. To illustrate, Figure 6 shows that as crustal thickness increases the relative axial depth within a segment generally decreases. There is a general agreement between the observations and the relative axial depth predicted solely by isostatic support, although there are exceptions. For example, along segment OH-2, relative axial depth is typically <500 m and does not appear to correlate with crustal thickness. One explanation may be that magmatism has recently waned (<10^5 years) resulting in a stronger axial lithosphere, in which case axial relief may be more affected by flexure than isostasy. Another exception to the trend is the Oceanographer fracture zone. In this region, higher densities in the mantle due to cooling across the fracture zone, serpentinized peridotites with a higher density than gabbros of the same velocity [*Miller and Christensen*, 1997], or dynamic effects near a ridge-transform intersection [e.g., *Phipps Morgan and Parmentier*, 1984; *Dick et al.*, 1991; *Bercovici et al.*, 1992] could each contribute to axial depths which are greater than predicted from seismically estimated crustal thickness and the assumption of isostasy.

As crustal thickness increases the upper bound on the relief of rift valley scarps generally decreases and the rift valley becomes narrower (Figure 7), confirming that thicker crust gives rise to weaker lithosphere with smaller faults [*Shaw*,

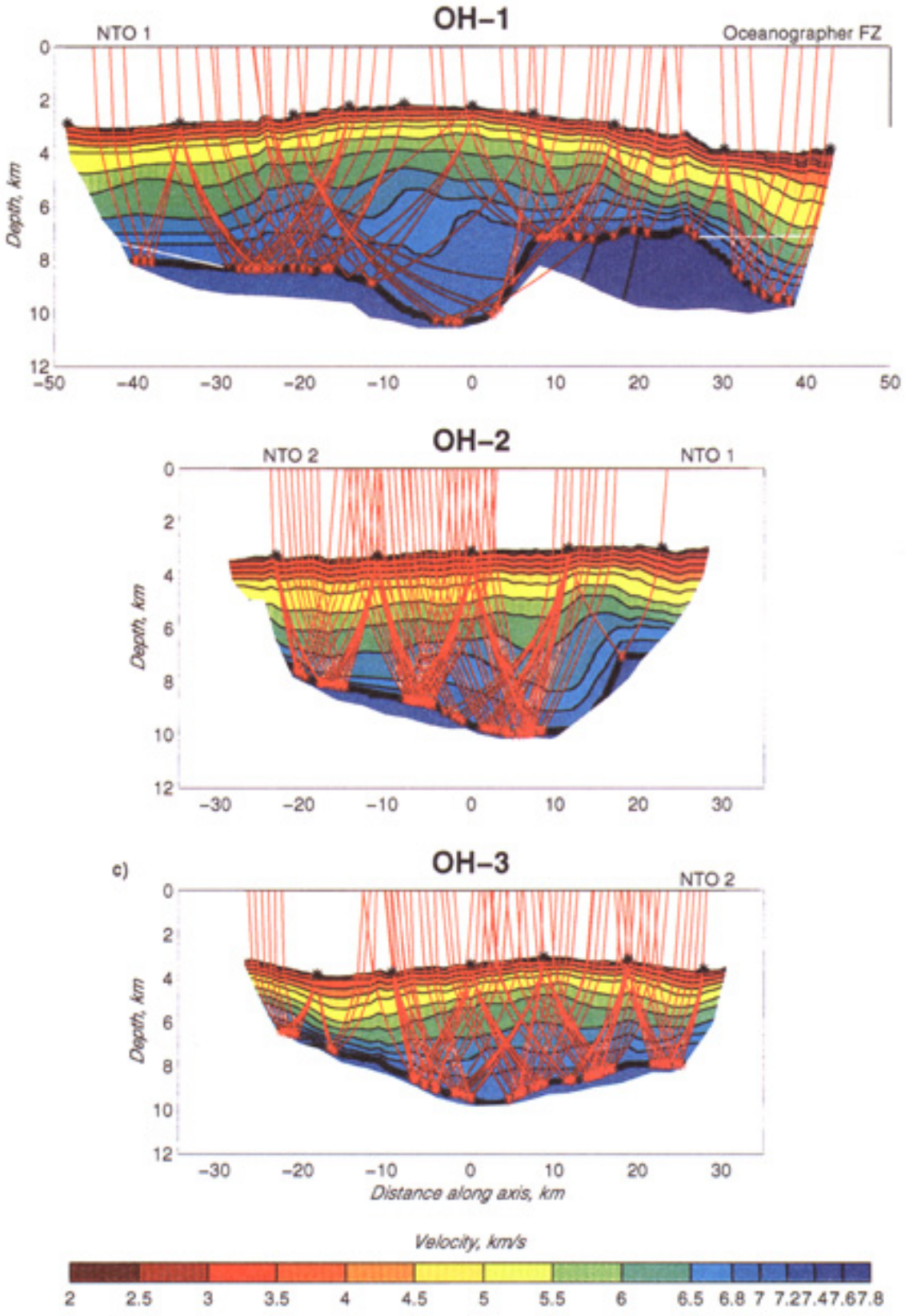

Plate 3. Final best fitting velocity models are shown. The Moho topography and the upper mantle velocities for the three segments (a) OH-1, (b) OH-2, and (c) OH-3 are determined by forward modelling of *Pg*, *PmP*, and *Pn* arrivals using the ray tracing scheme of *Zelt and Smith* [1992]. The parts of the velocity model that are not well resolved are masked. The portion of the Moho that is constrained by Moho reflections is shown by red stars and rays (every tenth ray used for OH-1 and every fifth ray used for OH-2 and OH-3). For segment OH-1 the white line represents the Moho topography adjusted at the segment ends to give a better fit to the gravity data. The seafloor OBHs are shown by stars.

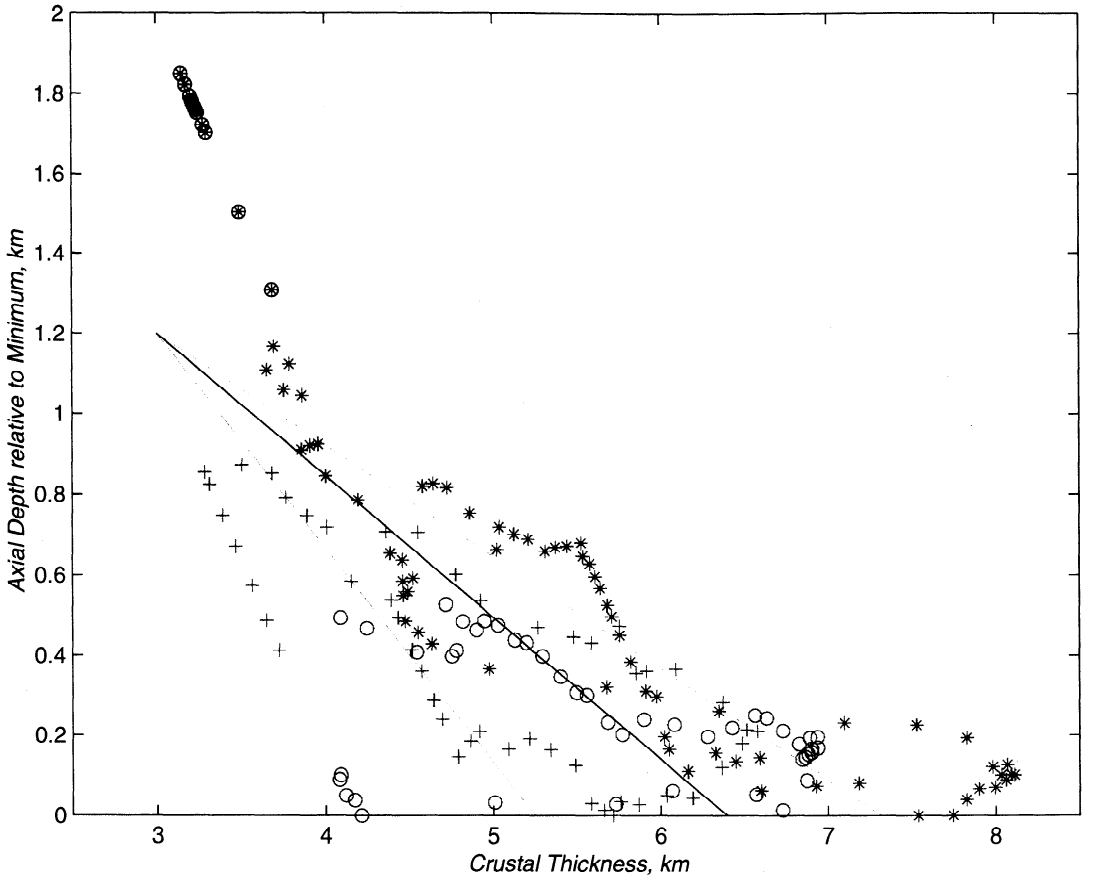

Figure 6. Axial depth relative to the minimum depth of the rift valley is plotted versus seismic crustal thickness for segment OH-1 (stars, with the Oceanographer fracture zone as circled stars; minimum depth is 2135 m), OH-2 (circles, minimum depth is 2847 m), and OH-3 (crosses, minimum depth is 2993 m). Also shown are curves for isostatically compensated crust with crustal densities of 2500 (thin line), 2700 (heavy line), and 2800 (dashed line) kg m^{-3} and a mantle density of 3300 kg m^{-3}. As crustal thickness increases the relative axial depth within a segment generally decreases.

1992; *Shaw and Lin*, 1993] and a narrow, shallow rift valley [*Chen and Morgan*, 1990; *Neumann and Forsyth*, 1993; *Shaw and Lin*, 1996]. For segment OH-2 or for crustal thickness <5 km, this trend is less well defined. From this we infer that crustal thickness alone does not govern lithospheric strength. Other processes that may affect rift valley morphology are three-dimensional effects that influence the propagation of faults along the ridge axis [*Shaw and Lin*, 1996] or variations in thermal structure that are out of phase or unassociated with the measured crustal thickness. Some factors that could influence the thermal structure are (1) the time elapsed since a major magmatic episode; (2) the effect of segment offset size; or (3) intersegment variations in magma plumbing (a centrally fed segment would presumably have a different thermal structure than one replenished along its entire length). Though we conclude that to first-order crustal thickness controls axial depth and lithospheric strength, other factors such as the thermal and dynamic consequences of ridge geometry, temporal and spatial patterns of magmatism, and serpentinization also play a role.

6.4. Is Segment OH-1 "Magmatically Robust" or "Robustly Focused"?

Previous studies suggested that segment OH-1 is "magmatically robust" in the sense that this segment's melt supply is anomalously high in comparison with other nearby segments. Evidence for this assertion includes its anomalously shallow axial depth, its anomalously low MBA, its geochemical anomaly [*Schilling*, 1986; *Shirey et al.*, 1987; *Schilling*, 1991; *Yu et al.*, 1997], and an unusual chain of seamounts, all near the segment's center [*Needham et al.*, 1992]. While we confirm that the flux of melt is greater near the center of segment OH-1 (relative to segments OH-2 and OH-3), we do not observe that the average melt flux per segment length is significantly different. This is in contrast to a similar segment at 33°S on the Mid-Atlantic Ridge where low $Na_{8.0}$ values indicate a greater extent of melting than beneath the adjacent segments [*Michael et al.*, 1994]. Our observations argue against an excess supply of melt over the length of segment OH-1 and instead favour a melt supply which, relative to nearby segments, is more strongly focused toward the segment center.

As discussed above, a mantle diapir can explain the observed intrasegment crustal thickness variations [*Lin et al.*, 1990; *Detrick et al.*, 1995]; however, another possibility is that the enhanced supply of melt at the segment center is due to focusing of melt at mantle depths in the absence of diapiric flow. From this point of view the greater crustal thickness at the center of segment OH-1 requires that melt be more efficiently and pervasively focused than at segments OH-2 and

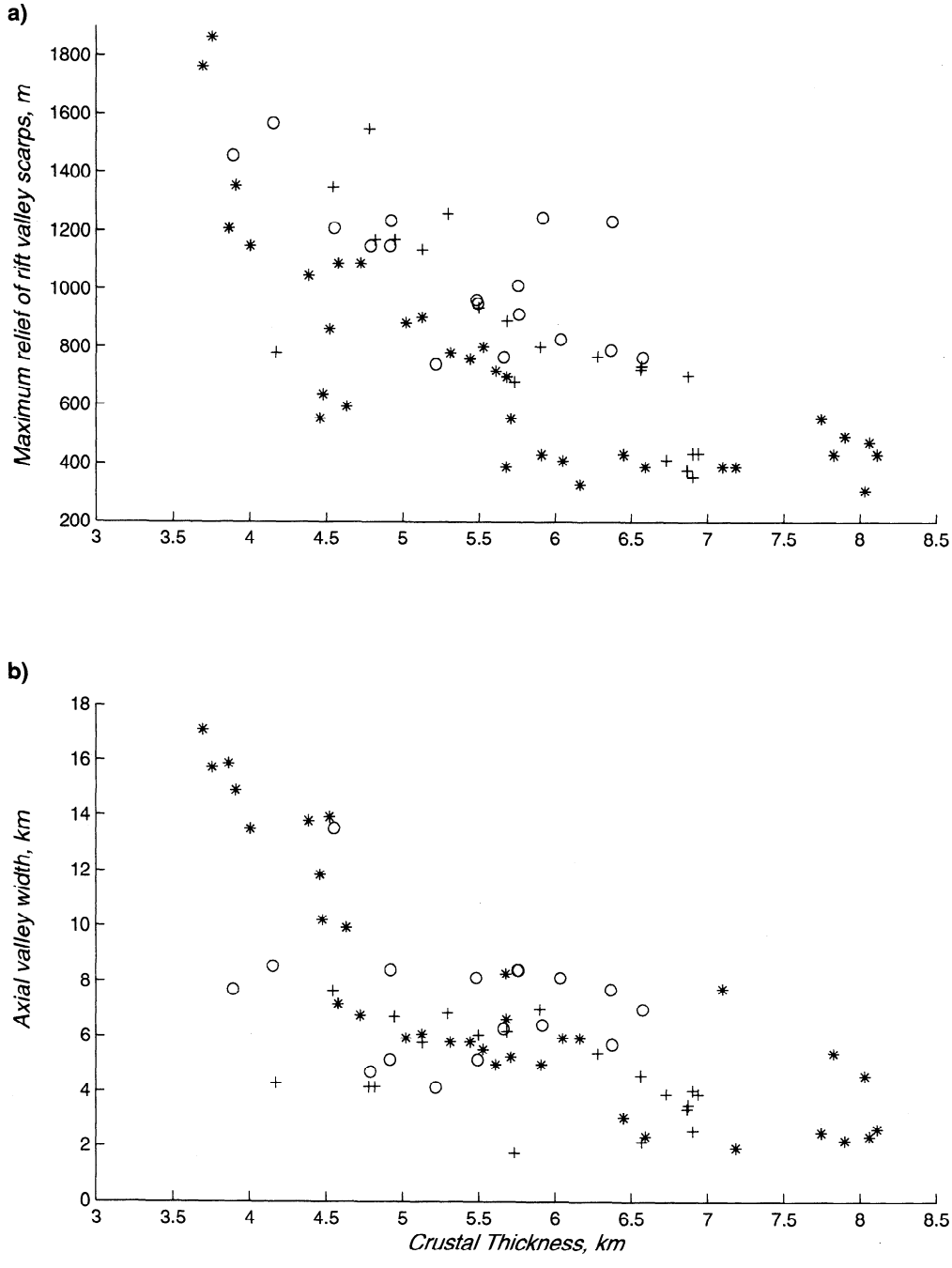

Figure 7. (a) The maximum relief of the eastern and western bounding scarps of the rift valley and (b) the rift valley width as a function of seismic crustal thickness for segments OH-1 (stars), OH-2 (circles), and OH-3 (crosses) are shown. The rift valley scarps are defined as the first steep slopes of the rift valley walls and were picked every 1 km along axis. In assessing the influence of crustal thickness on lithospheric strength, the scarps are used as a proxy for the rift valley bounding faults. The rift valley width is determined as the distance between the base of the rift valley scarps. Measurements within 7 km of the Oceanographer fracture zone were excluded. Thicker crust is generally associated with smaller rift valley scarps and a narrow, shallow rift valley.

OH-3 (Figure 8). This difference indicates that segment length and offset affect the transport/focusing of melt from the melting region to where it is emplaced in the crust. The physical processes controlling mantle melt migration are not well understood; however, melt focusing may occur along a thermally controlled boundary [e.g., *Sparks and Parmentier*, 1994; *Magde et al.*, 1997]. In the case of segment OH-1 the steep mantle isotherms due to the presence of the Oceanographer fracture zone [*Detrick et al.*, 1995; *Magde et al.*, 1997] would result in more extensive focusing of melt to the segment center than at nontransform offsets where relief on mantle isotherms is more subdued. Thus strong lateral migration of melt away from the Oceanographer fracture zone may help generate the anomalously thick crustal root and the accompanying seamount chain. A dominant influence of the fracture zone thermal structure on melt migration would also

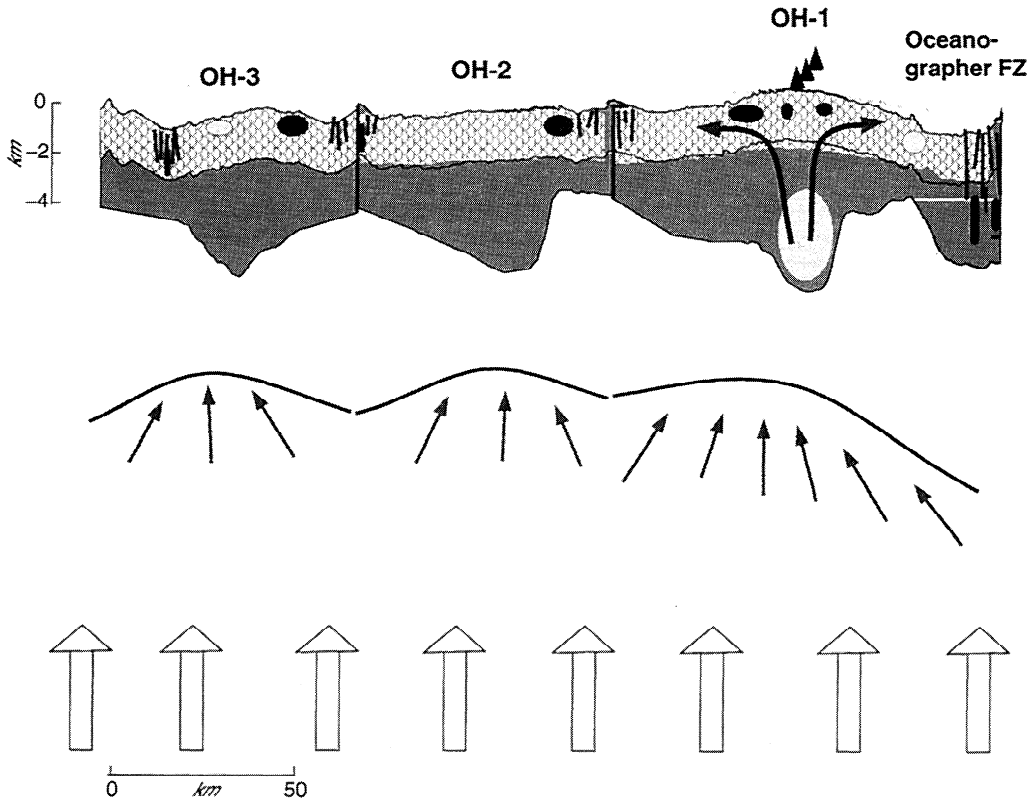

Figure 8. Summary cartoon of the crustal and mantle structure along the axis of the three ridge segments. There are intersegment and intrasegment variations in crustal thickness, shown bounded at the top by the seafloor and at the bottom by the Moho (shaded). Surprisingly, the average crustal thickness for these three segments is similar, implying that the melt produced per segment length is constant. At segment OH-1, melt is focused to the segment center in the mantle (arrows) generating thick crust relative to the segment ends, a seamount chain (triangles), and a low-velocity zone in the lower crust (light shading). At midcrustal depths melt is redistributed along axis, probably by lateral dike injections controlled by the brittle-ductile transition. The upper crust (scalloped pattern) has a relatively uniform thickness along axis but has internal heterogeneities (high and low velocities are indicated by dark and light shading, respectively). At the segment ends, fracturing (lines) and serpentinization control the crustal structure (dark ovals). The white line at the Oceanographer fracture zone indicates the Moho topography adjusted to fit the gravity data.

explain the observation that the distance between the seamount chain and the Oceanographer fracture zone has remained constant in spite of the southward growth of this segment over the last 5 Myr [*Deplus et al.*, 1998]. Last, as fracture zone offset grows, the effect of steeper mantle isotherms on melt migration could explain the observed correlation between the axial variation in MBA amplitude and segment offset [*Detrick et al.*, 1995]. This model implies that the anomalous geochemical signature at segment OH-1 is not linked to excess melting. By the melt focusing view, the "magma budget" of a particular ridge cross section need not imply the amount of melt produced in the underlying mantle but rather the amount of melt delivered to a crustal section.

7. Summary

We present results from the Mid-Atlantic Ridge Bull's Eye Experiment, a seismic refraction experiment that determined the thickness and seismic structure of the crust and mantle at three contrasting spreading segments, OH-1, OH-2, and OH-3. The main results from this study are as follows:

1. There are significant along-axis variations in crustal thickness along the three ridge segments. Crustal thickness at the segment center decreases from north to south (8.1, 6.9, and 6.6 ±0.5 km) and correlates with the observed reduction in mantle Bouguer anomaly gravity low. Crustal thickness at the segment ends is 2.5 to 5 ±0.5 km and does not correlate with segment length or offset. To first order, crustal thickness appears to control axial depth and the characteristic morphology of the rift valley; however, other thermal and dynamic factors may also play a role.

2. At the segment center, the velocity structure is typical for oceanic crust. At the segment ends, low upper crustal velocities and linear velocity-depth gradients in the fracture zone and nontransform nodal basins indicate that alteration and fracturing of a thin basaltic crust and underlying mantle control the velocity structure. Large-scale faulting may also be important at the segment ends, particularly at the Oceanographer fracture zone.

3. Away from the segment ends the thickness of the upper crustal units is relatively uniform though internally heterogeneous, with high- and low-velocity regions (~±0.6

km s^{-1} over scales of ~5 km and down to 3 km depth). These bodies may indicate the size of volcanic units and the observed lateral variability points to temporally and spatially distinct accretionary events within the axial valley.

4. The enhanced flux of mantle melt to segment centers results in a lower crust which is thickest at the segment centers and the presence of partial melt in the crustal root at segment OH-1. At midcrustal depths, our results from segment OH-1, in conjunction with other studies, indicate that melt is redistributed by lateral dike injection, possibly controlled by the brittle-ductile transition.

5. We find that the average crustal thickness is similar at each segment (5.6±0.4, 5.7±0.4, and 5.1±0.3 km, from north to south), particularly if a regional trend due to the waning influence of the Azores hotspot is removed. This indicates that the melt flux per segment length is constant. In the case of segment OH-1 this argues against excess melting of the mantle and instead favors a melt supply which, relative to nearby segments, is more strongly focused toward the segment center. We suggest a dominant influence of the thermal structure of the Oceanographer fracture zone on melt migration in the mantle.

Appendix

Two resolution tests were performed to test the robustness of the velocity anomalies observed in the shallow crust. In the first resolution test a high- and a low-velocity body (±0.6 km s^{-1}, 1-3 km depth, 20 km long, 2 km wide) were superimposed on a velocity structure that varied only with depth (Figure A1). This was done to examine the amplitude recovery and depth resolution of lateral velocity variations similar to those that we observe. Normal noise was added to travel times predicted for this velocity model, and these data were then inverted using the one-dimensional velocity depth model as a starting model and high spatial smoothing parameters. Lateral and vertical recovery was good with some spreading of the recovered structures due to the high smoothing used. The

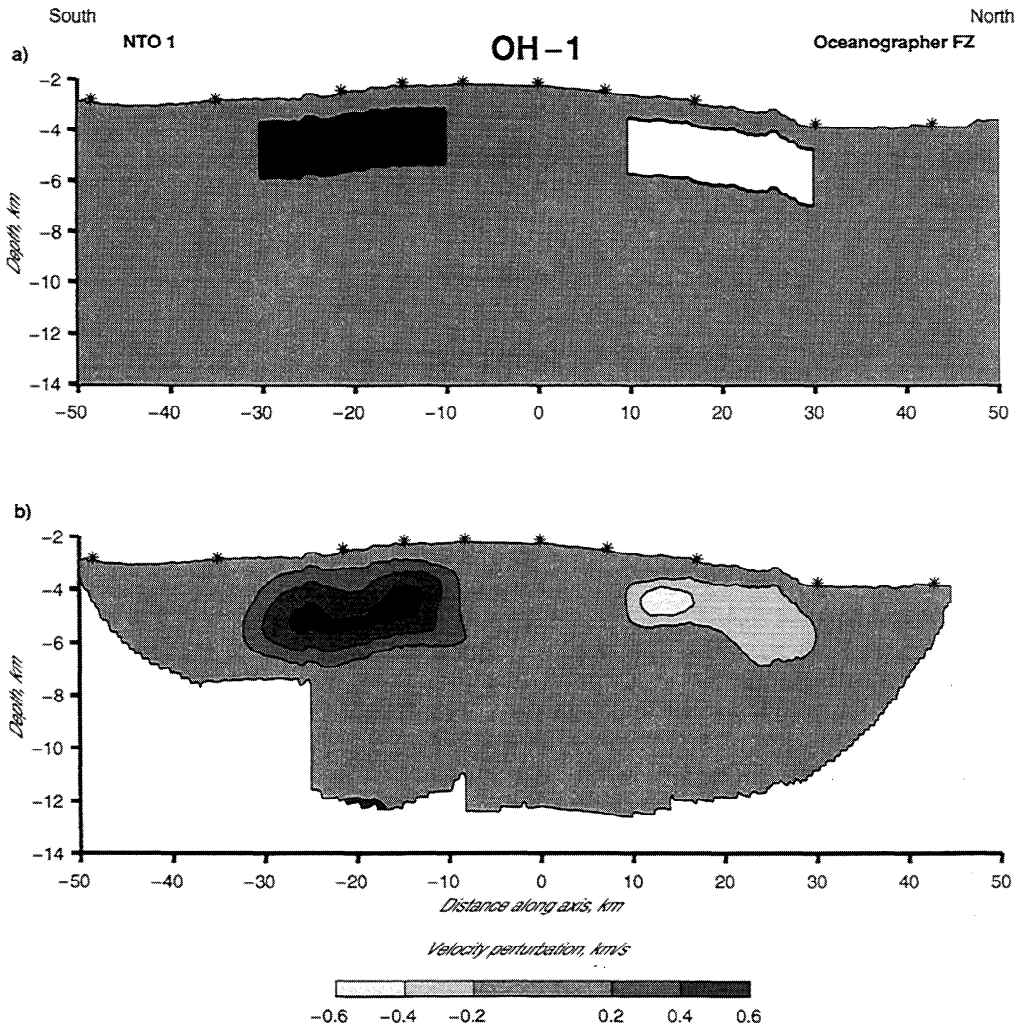

Figure A1. Resolution test is shown for the variability in velocity structure within the upper crust at segment OH-1. (top) Positive and negative velocity perturbations that were added to a linear velocity depth gradient (±0.6 km s^{-1}, 1-3 km depth, 20 km long and 11 km wide) are shown. Synthetic travel times were calculated for this velocity model, normal noise was added, and these data were inverted tomographically. (bottom) Recovered velocity perturbations for the ray coverage in our experiment are shown; see text for discussion. Horizontal and vertical spatial smoothing parameters were both high (1000).

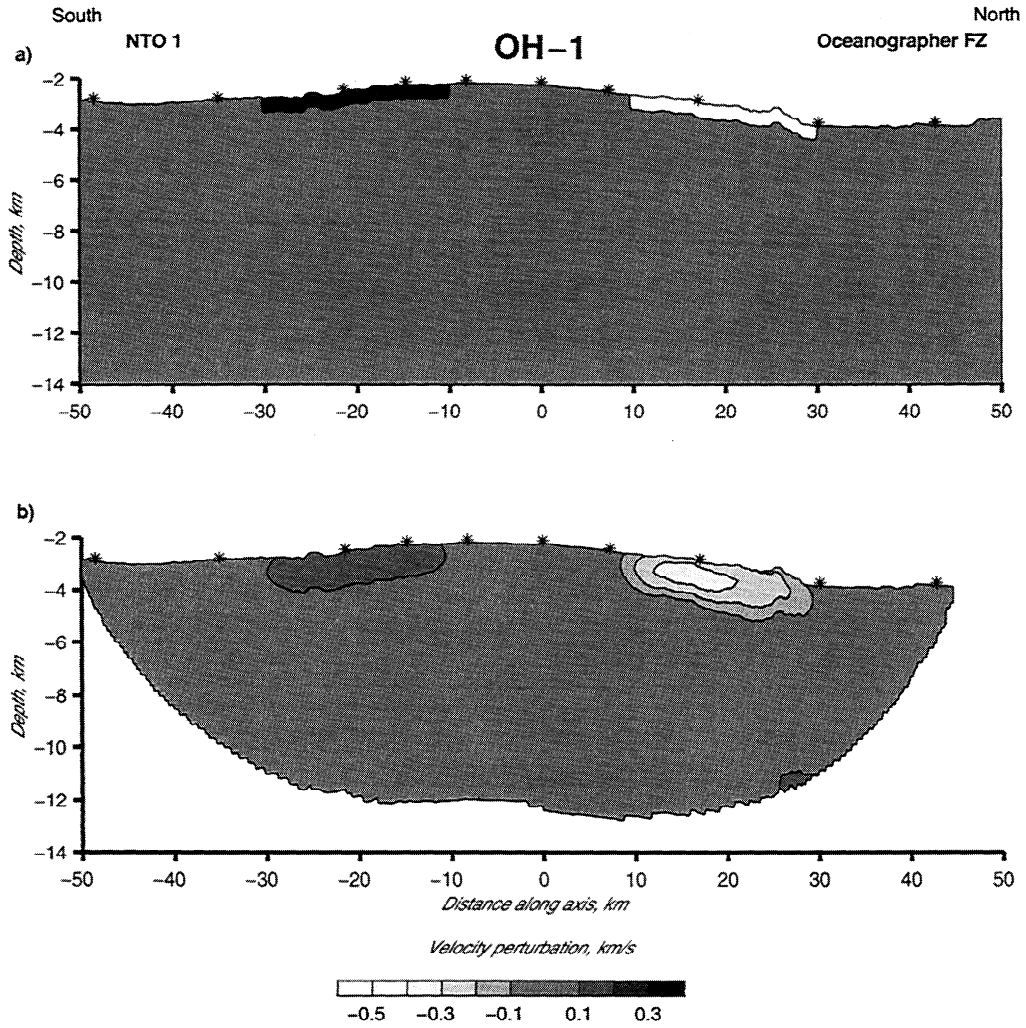

Figure A2. Resolution test for the effect of surficial crustal velocity perturbations at segment OH-1. (top) Positive and negative velocity perturbations that were added to a linear velocity depth gradient (+0.4 km s^{-1} and -0.6 km s^{-1}, seafloor to 500 m depth, 20 km long and 2 km wide) are shown. (bottom) Recovered velocity preturbations are shown; see Figure A1 caption.

low-velocity body was somewhat reduced in size, and amplitude recovery was better in the third of the body that had more dense ray coverage. The high-velocity body was shifted to somewhat deeper depths ~500 m and was more spread out with good amplitude recovery.

In a similar manner, we tested a second velocity structure which consisted of a high- (+0.4 km s^{-1}) and low- (-0.6 km s^{-1}) velocity body at the seafloor (both are 500 m thick, 20 km along axis, 5 km wide) (Figure A2). This was to examine whether the variations in seafloor velocity observed in multichannel analyses (S.A. Hussenoeder et al., Upper crustal seismic structure of the slow spreading Mid-Atlantic Ridge, 35°N: Constraints on volcanic emplacement processes, submitted to *Journal of Geophysical Research*, 1999) are smeared down into the rest of layer 2 by the tomographic inversion. Again, lateral recovery of these anomalies is very good. The recovered velocities are averaged over the upper 1 km due to the lack of crossing rays in this depth range. As a result, the high-velocity body is resolved as a high of magnitude 0.2 km s^{-1} extending over the upper 1 km, and the low is resolved as a body of anomaly -0.3 km s^{-1} extending over the upper 1.5-1.75 km. Slight further smearing of these structures occurs due to the high spatial smoothing values used. These results are entirely as expected from the ray geometry and inversion parameters, and the surficial velocities variations do not generate artificial structures deeper in layer 2 (i.e., >1-2 km depth).

Acknowledgments. We thank Captain I. Young, Science Officer J. Stennet, and the crew of the R/V *Maurice Ewing* Leg 96-08 for data acquisition. We are grateful to the WHOI OBS group J. Bailey, J. Dolan, D. Dubois, J. Hallinan, and B. Wooding for their technical support. A. Hosford generated the bathymetry maps. This study benefited from discussions with A. Barclay, J.P. Canales, and L. Magde. We thank R. Carlson, R. White, and D. Sparks for constructive reviews. E.E.E.H. was supported by a postdoctoral fellowship at the Department of Terrestrial Magnetism, Carnegie Institution of Washington, D.C. This work was supported by NSF grant OCE-9300450 to the Woods Hole Oceanographic Institution and NSF grants EIA-9601802 and ACI-9522531 to the University of Oregon.

References

Barclay, A.H., D.R. Toomey, and S.C. Solomon, Seismic structure and

crustal magmatism at the Mid-Atlantic Ridge, 35°N, *J. Geophys. Res.*, *103*, 17,827-17,844, 1998.

Bercovici, D., H.J.B. Dick, and T. Wagner, Nonlinear viscoelasticity and the formation of transverse ridges, *J. Geophys. Res.*, *97*, 14,195-14,206, 1992.

Bideau, D., R. Hékinian, C. Bollinger, M. Constantin, E. Gàrcia, C. Guivel, B. Sichler, R. Apprioual, and R. Le Gall, Submersible investigation of highly contrasted magmatic activities recorded on two segments of the Mid-Atlantic Ridge near 34°25'N and 33°55'N, *InterRidge News*, *5*, 9-14, 1996.

Blackman, D.K., and D.W. Forsyth, Isostatic compensation of tectonic features of the Mid-Atlantic Ridge: 25°-27°30'S, *J. Geophys. Res.*, *96*, 11,741-11,758, 1991.

Brandsdóttir, B., W. Menke, P. Einarsson, R.S. White, and R.K. Staples, Färoe-Iceland Ridge Experiment, 2, Crustal structure of the Krafla central volcano, *J. Geophys. Res.*, *102*, 7867-7886, 1997.

Canales, P., R.S. Detrick, J. Lin, J.A. Collins, and D.R. Toomey, Crustal and upper mantle seismic structure beneath the Rift Mountains and across a nontransform offset at the Mid-Atlantic Ridge (35°N), *J. Geophys. Res.*, *105*, 2699-2719, 2000.

Cannat, M., Emplacement of mantle rocks in the seafloor at mid-ocean ridges, *J. Geophys. Res.*, *98*, 4163-4172, 1993.

Carlson, R.L., and G.S. Raskin, Density of the ocean crust, *Nature*, *311*, 555-558, 1984.

Chen, Y., and W.J. Morgan, A nonlinear rheology model for mid-ocean ridge axis topography, *J. Geophys. Res.*, *95*, 17,583-17,604, 1990.

Christensen, N.I., Compressional wave velocities in rocks at high temperatures and pressures, critical thermal gradients, and crustal low-velocity zones, *J. Geophys. Res.*, *84*, 6849-6857, 1979.

Crane, K., The spacing of rift axis highs: Dependence upon diapiric processes in the underlying asthenosphere?, *Earth Planet. Sci. Lett.*, *72*, 405-414, 1985.

Creager, K.C., and L.M. Dorman, Location of instruments on the seafloor by joint adjustment of instrument and ship positions, *J. Geophys. Res.*, *87*, 8379-8388, 1982.

DeMets, C., R.G. Gordon, D.F. Argus, and S. Stein, Current plate motions, *Geophys. J. Int.*, *101*, 425-478, 1990.

Deplus, C., et al., Linking variation in magma supply and segment growth: Temporal evolution of segment OH-1 (MAR at 35°N) during the last 12 Myr, *Eos Trans. AGU*, *79* (45), Fall Meet. Suppl., 856, 1998.

Detrick, R.S., R.S. White, and G.M. Purdy, Crustal structure of north Atlantic fracture zones, *Rev. Geophys.*, *31*, 439-458, 1993.

Detrick, R.S., H.D. Needham, and V. Renard, Gravity anomalies and crustal thickness variations along the Mid-Atlantic Ridge between 33°N and 40°N, *J. Geophys. Res.*, *100*, 3767-3787, 1995.

Detrick, R., J. Collins, G. Kent, J. Lin, D. Toomey, A. Barclay, E. Hooft, A. Hosford, and S. Hussenoeder, Mid-Atlantic Ridge Bull's Eye experiment: A seismic investigation of segment-scale crustal heterogeneity at a slow-spreading ridge, *InterRidge News*, *6*, 27-32, 1997.

Dick, H.J.B., et al., Tectonic evolution of the Atlantis II fracture zone, *Proc. Ocean Drill. Program Sci. Results*, *118*, 359-398, 1991.

Dick, H.J.B., P.T. Robinson, and P. Meyer, The plutonic foundation of a slow-spreading ridge, in *Synthesis of Results from Scientific Drilling in the Indian Ocean, Geophys. Monogr. Ser.*, vol. 70, edited by R. Duncan and D. Rea, pp. 1-39, AGU, Washington D.C., 1992.

Dunn, R.A., and D.R. Toomey, Seismological evidence for three-dimensional melt migration beneath the East Pacific Rise, *Nature*, *388*, 259-262, 1997.

Dziak, R.P., C.G. Fox, and A.E. Schreiner, The June-July 1993 seismo-acoustic event at the CoAxial segment, Juan de Fuca Ridge: Evidence for a lateral dike injection, *Geophys. Res. Lett.*, *22*, 135-138, 1995.

Einarsson, P., and B. Brandsdóttir, Seismological evidence for lateral magma intrusion during the July 1978 deflation of the Krafla volcano in NE Iceland, *J. Geophys.*, *47*, 160-165, 1980.

Escartín, J., and J. Lin, Ridge offsets, normal faulting, and gravity anomalies of slow spreading ridges, *J. Geophys. Res.*, *100*, 6163-6177, 1995.

Fowler, C.M.R., Crustal structure of the Mid-Atlantic Ridge crest at 37°N, *Geophys. J. R. Astron. Soc.*, *47*, 459-491, 1976.

Fowler, C.M.R., The Mid-Atlantic Ridge: Structure at 45°N, *Geophys. J. R. Astron. Soc.*, *54*, 167-183, 1978.

Fox, P.J., E. Schreiber, H. Rowlett, and K. McCamy, The geology of the Oceanographer Fracture Zone: A model for fracture zones, *J. Geophys. Res.*, *81*, 4117-4128, 1976.

Gràcia, E., D. Bideau, R. Hékinian, Y. Lagabrielle, and L.M. Parson, Along-axis magmatic oscillations and exposure of ultramafic rocks in a second-order segment of the Mid-Atlantic Ridge (33°43'N to 34°07'N), *Geology*, *25*, 1059-1062, 1997.

Keen, C., and C. Tramontini, A seismic refraction survey on the Mid-Atlantic Ridge, *Geophys. J. R. Astron. Soc.*, *20*, 473-491, 1970.

Kelemen, P.B., N. Shimizu, and V.J.M. Salters, Extraction of mid-ocean-ridge basalt from upwelling mantle by focused melt in dunite channels, *Nature*, *375*, 747-753, 1995.

Kincaid, C., D.W. Sparks, and R.S. Detrick, The relative importance of plate-driven and buoyancy-driven flow at mid-ocean ridges, *J. Geophys. Res.*, *101*, 16,177-16,193, 1996.

Kong, L.S., S.C. Solomon, and G.M. Purdy, Microearthquake characteristics of a mid-ocean ridge along-axis high, *J. Geophys. Res.*, *97*, 1659-1685, 1992.

Koyanagi, R.Y., W.R. Tanigawa, and J.S. Nakata, Seismicity associated with the eruption, in *The Puu Oo Eruption of Kilauea Volcano, Hawaii: Episodes 1 through 2, January 3, 1983, through June 8, 1984, U.S. Geol. Surv. Prof_Pap., 1463*, 183-235, 1988.

Kuo, B.-Y., and D.W. Forsyth, Gravity anomalies of the ridge-transform system in the South Atlantic between 31° and 34.5°S: Upwelling centers and variations in crustal thickness, *Mar. Geophys.Res.*, *10*, 205-232, 1988.

LeDouaran, S., H.D. Needham, and J. Francheteau, Pattern of opening rates along the axis of the Mid-Atlantic Ridge, *Nature*, *300*, 254-257, 1982.

Lin, J., and J. Phipps Morgan, The spreading rate dependence of three-dimensional mid-ocean ridge gravity signature, *Geophys. Res. Lett.*, *19*, 13-16, 1992.

Lin, J., G.M. Purdy, H. Schouten, J.-C. Sempere, and C. Zervas, Evidence from gravity data for focused magmatic accretion along the Mid-Atlantic Ridge, *Nature*, *344*, 627-632, 1990.

Magde, L.S., and D.W. Sparks, Three-dimensional mantle upwelling, melt generation and melt migration beneath segmented slow-spreading ridges, *J. Geophys. Res.*, *102*, 20,571-20,583, 1997.

Magde, L.S., D.W. Sparks, and R.S. Detrick, The relationship between buoyant mantle flow, melt migration, and gravity bull's eyes at the Mid-Atlantic Ridge between 33°N and 35°N, *Earth Planet. Sci. Lett.*, *148*, 59-67, 1997.

Magde, L.S., A.H. Barclay, and D.R. Toomey, Crustal magma plumbing within a segment of the Mid-Atlantic Ridge, 35°N, *Earth Planet. Sci. Lett.*, in press, 2000.

Michael, P.J., et al., Mantle control of a dynamically evolving spreading center: Mid-Atlantic Ridge 31-34°S, *Earth Planet. Sci. Lett.*, *121*, 451-468, 1994.

Miller, D.J., and N.I. Christensen, Seismic velocities of lower crustal and upper mantle rocks from the slow-spreading Mid-Atlantic Ridge, south of the Kane Transform Zone (MARK), *153*, 437-451, 1997.

Morris, E., and R.S. Detrick, Three-dimensional analysis of gravity anomalies in the MARK area, Mid-Atlantic Ridge 23°N, *J. Geophys. Res.*, *96*, 4355-4366, 1991.

Moser, T.J., Shortest path calculation of seismic rays, *Geophysics*, *56*, 59-67, 1991.

Mutter, J., and J. Karson, Structural processes at slow spreading ridges, *Science*, *257*, 627-634, 1992.

Needham, H.D., M. Voisset, D. Renard, H. Bougault, O. Dauteuil, R. Detrick, and C. Langmuir, Structural and volcanic features of the Mid-Atlantic rift zone between 40°N and 33°N, *Eos Trans. AGU*, *73* (43), Fall Meet. Suppl., 552, 1992.

Neumann, G.A., and D.W. Forsyth, The paradox of the axial profile: Isostatic compensation along the axis of the mid-Atlantic ridge?, *J. Geophys. Res.*, *98*, 17,891-17,910, 1993.

Okubo, P.G., H.M. Benz, and B.A. Chouet, Imaging the crustal magma source beneath Mauna Loa and Kilauea volcanoes, Hawaii, *Geology*, *25*, 867-870, 1997.

Parker, R.L., The rapid calculation of potential anomalies, *Geophys. J. R. Astron. Soc.*, *31*, 447-455, 1972.

Phipps Morgan, J., and D.W. Forsyth, Three-dimensional flow and temperature perturbations due to a transform offset: Effects on oceanic crustal and upper mantle structure, *J. Geophys. Res.*, *93*, 2955-2966, 1988.

Phipps Morgan, J., and E.M. Parmentier, Lithospheric stress near a ridge-transform intersection, *Geophys. Res. Lett.*, *11*, 113-116, 1984.

Purdy, G.M., and R.S. Detrick, Crustal structure of the Mid-Atlantic Ridge at 23°N from seismic refraction studies, *J. Geophys. Res.*, *91*, 3739-3762, 1986.

Reynolds, J., and C. Langmuir, Petrological systematics of the Mid-Atlantic Ridge south of Kane: Implications for ocean crust formation, *J. Geophys. Res.*, *102*, 14,915-14,946, 1997.

Rubin, A.M., D. Gillard, and J.-L. Got, A reinterpretation of seismicity associated with the January 1983 dike intrusion at Kilauea Volcano, Hawaii, *J. Geophys. Res.*, *103*, 10,003-10,015, 1998.

Schilling, J.-G., Geochemical and isotopic variation along the Mid-Atlantic Ridge axis from 79°N to 0°N, in *The Geology of North America,* vol. M, *The Western North Atlantic*, edited by B. E. Tucholke and P. R. Vogt, pp. 137-156, Geol. Soc. of Am., Boulder, Colo., 1986.

Schilling, J.-G., Fluxes and excess temperatures of mantle plumes inferred from their interaction with migrating mid-ocean ridges, *Nature*, *352*, 397-403, 1991.

Schouten, H., and R.S. White, Zero offset fracture zones, *Geology*, *8*, 175-179, 1980.

Schouten, H., K.D. Klitgord, and J.A. Whitehead, Segmentation of mid-ocean ridges, *Nature*, *317*, 225-229, 1985.

Sempéré, J.-C., G.M. Purdy, and H. Schouten, Segmentation of the Mid-Atlantic Ridge between 24°N and 30°40'N, *Nature*, *344*, 427-431, 1990.

Shaw, P., Ridge segmentation, faulting and crustal thickness in the Atlantic Ocean, *Nature*, *358*, 490-493, 1992.

Shaw, P.R., and J. Lin, Causes and consequences of variations in faulting style at the Mid-Atlantic Ridge, *J. Geophys. Res.*, *98*, 21,839-21,851, 1993.

Shaw, W.J., and J. Lin, Models of ocean ridge lithospheric deformation: Dependence on crustal thickness, spreading rate, and segmentation, *J. Geophys. Res.*, *101*, 17,977-17,993, 1996.

Shirey, S.B., J.F. Bender, and C.H. Langmuir, Three-component isotopic heterogeneity near the Oceanographer transform, Mid-Atlantic Ridge, *Nature*, *325*, 217-223, 1987.

Sinha, M.C., and K.E. Louden, The Oceanography fracture zone, I, Crustal structure from seismic refraction studies, *Geophys. J. R. Astron. Soc.*, *75*, 713-736, 1983.

Sparks, D.W., and E.M. Parmentier, The structure of three-dimensional convection beneath oceanic spreading centers, *Geophys. J. Int.*, *112*, 81-91, 1993.

Sparks, D.W., and E.M. Parmentier, The generation and migration of partial melt beneath oceanic spreading centers, in *Magmatic Systems,* edited by M.P. Ryan, pp. 55-76, Academic , San Diego, Calif., 1994.

Sparks, D.W., E.M. Parmentier, and J. Phipps Morgan, Three-dimensional mantle convection beneath a segmented spreading center: Implications for along-axis variations in crustal thickness and gravity, *J. Geophys. Res.*, *98*, 21,977-21,995, 1993.

Tolstoy, M., A.J. Harding, and J.A. Orcutt, Crustal thickness on the Mid-Atlantic Ridge: Bull's eye gravity anomalies and focused accretion, *Science*, *262*, 726-729, 1993.

Toomey, D.R., and G.R. Foulger, Tomographic inversion of local earthquake data from the Hengill-Grensdalur central volcano complex, Iceland, *J. Geophys. Res.*, *94*, 17,497-17,510, 1989.

Toomey, D.R., S.C. Solomon, G.M. Purdy, and M.H. Murray, Microearthquakes beneath the median valley of the Mid-Atlantic Ridge near 23°N: Hypocenters and focal mechanisms, *J. Geophys. Res.*, *90*, 5443-5485, 1985.

Toomey, D.R., S.C. Solomon, and G.M. Purdy, Microearthquakes beneath the median valley of the Mid-Atlantic Ridge near 23°N: Tomography and tectonics, *J. Geophys. Res.*, *93*, 9093-9112, 1988.

Toomey, D.R., G.M. Purdy, S.C. Solomon, and W.S.D. Wilcock, The three-dimensional seismic velocity structure of the East Pacific Rise near latitude 9°30'N, *Nature*, *347*, 639-645, 1990.

Toomey, D.R., S.C. Solomon, and G.M. Purdy, Tomographic imaging of the shallow crustal structure of the East Pacific Rise at 9°320'N, *J. Geophys. Res.*, *99*, 24,135-24,157, 1994.

Tucholke, B.E., and J. Lin, A geological model for the structure of segments in slow spreading ocean crust, *J. Geophys. Res.*, *99*, 11,937-11,959, 1994.

White, R.S., R.S. Detrick, M.C. Sinha, and M.H. Cormier, Anomalous seismic crustal structure of oceanic fracture zones, *Geophys. J. R. Astron. Soc.*, *79*, 779-798, 1984.

White, R.S., D. McKenzie, and K. O'Nions, Oceanic crustal thickness from seismic measurements and rare earth element inversions, *J. Geophys. Res.*, *97*, 19,683-19,716, 1992.

Whitehead, J.A., H.J.B. Dick, and H. Schouten, A mechanism for magmatic accretion under spreading centers, *Nature*, *312*, 146-147, 1984.

Wolfe, C.J., G.M. Purdy, D.R. Toomey, and S.C. Solomon, Microearthquake characteristics and crustal velocity structure at 29°N on the Mid-Atlantic Ridge: The architecture of a slow spreading segment, *J. Geophys. Res.*, *100*, 24,449-24,472, 1995.

Yu, D., D. Fonignie, and J.-G. Schilling, Mantle plume-ridge interactions in the central North Atlantic: A Nd isotope study of Mid-Atlantic Ridge basalts from 30°N to 50°N, *Earth Planet. Sci. Lett.*, *146*, 259-272, 1997.

Zelt, C.A., and R.B. Smith, Seismic travel time inversion for 2-D crustal velocity structure, *Geophys. J. Int.*, *108*, 16-34, 1992.

J.A. Collins, R.S. Detrick, and J. Lin, Department of Marine Geology and Geophysics, Woods Hole Oceanographic Institution, Woods Hole, MA 02543. (jcollins@whoi.edu, rdetrick@whoi.edu, jlin@whoi.edu)

E.E.E. Hooft and D.R. Toomey, Department of Geological Sciences, University of Oregon, Eugene, OR 97403. (emilie@newberry.uoregon.edu, drt@newberry.uoregon.edu)

(Received February 12, 1999; revised October 11, 1999;
accepted December 17, 1999.)